POLITECNICO DI MILANO

DEPARTMENT OF PHYSICS

DOCTORAL PROGRAM IN PHYSICS

Silicon-Germanium Heterostructures for Silicon Photonics Applications

Doctoral Dissertation of:

Jacopo Frigerio

Supervisor:

Dr. Giovanni Isella

Tutor:

Prof. Franco Ciccacci

The Chair of the Doctoral Program:

Prof. Paola Taroni

2014 - XXVI Cycle

Contents

Introduction

Silicon photonics addresses the study and the technological application of silicon as an optical medium for generation, transmission, modulation and detection of light. It has been envisioned that silicon photonics will solve the interconnect bottleneck of CMOS technology, by the on-chip integration of silicon based optical interconnects with standard electronic elements. This technology has already shown its tremendous potential in the first demonstration of board-to-board optical interconnetion [1] in which an integrated transmitter chip with hybrid silicon lasers and an integrated receiver chip based on germanium photodetectors were connected by optical fibers to realize a 50 Gbit s^{-1} optical link. Nowadays, commercially-available Si-based 100 Gbit s^{-1} optical transceiver are the first choise for data communication in server clusters or data storage centers [2],[3], neverthless, the on-chip integration of silicon photonics still remains far to be reached. First of all, energy consumption targets for optical modulators are very aggressive, 100 fJ/bit for off-chip distances, 10's of fJ/bit for high density off-chip connections and a few fJ/bit for on-chip applications [4]. Wideband silicon modulators based on the Mach-Zender architecture typically have much larger energy compsumption due to the large device size [5],[6] and new low-energy approches involving electro-optic polymers still suffers of high insertion losses and temperature sensitivity. Moreover, for future on-chip optical applications, an efficient, monolithically integrated laser source is required. A Ge-on-Si laser source has already been demonstrated both in optical [7] and electrical [8] pumping configuration, nevertheless the threshold current and the output

power are still far from the required values for on-chip applications [9]. In the last decade, the envisioned integration of optics and electronics has driven a remarkable developement of silicon and germanium-on-silicon technology, opening new paths for applications not related to interconnetions, such as optical sensors for biological applications [10] and solar cells. The first aim of this thesis is to study and develop high performance and low-energy intensity and phase modulators based on Ge/SiGe multiple quantum wells (MQW) by exploiting the Quantum Confined Stark Effect. The presented results show that Ge/SiGe MQW have a strong potential as a new possible material platform for the future developement of silicon photonics.The second aim is the developement of highly tensile strained Ge-on-Si devices for efficent light emission.

The interconnect bottleneck

With the developement of the 22 nm Intel Tri-Gate Transistor Technology [11] (See. Fig1), the Moore law will be respected for many years to come, nevertheless, the electrical interconnection problem is expected to became a major limitation within a few years. The first problem to be considered in relation to the electrical wiring is the interconnect density. As the complexity of the

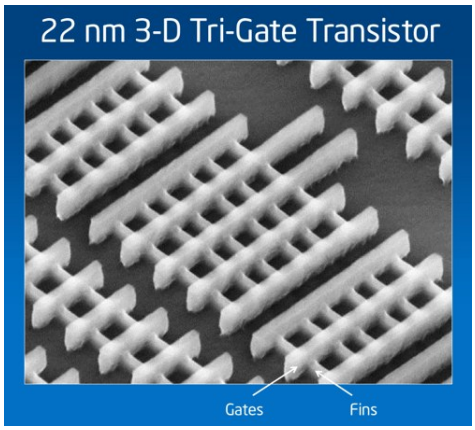

Figure 1: Image of the 22nm 3D Tri-Gate transistor. Source: Intel website.

integrated circuit increases, the available space tends to be filled with wiring and as a consequence, their dimensions have to be scaled, but the capacity of the wire in terms of transmission capacity cannot increase. This limitation can be understood in terms of a simple physical model. At the gigahertz working frequency typical of modern integrated circuits, interconnections are mainly limited by their RC product. If the cross-sectional size of the wire is reduced, its resistance will increase. Moreover, the capacitance per unit-lenght will remain unchanged, since it scales only logarithmically with the ratio of the wire size to wire separation. Briefly, by scaling the wires in all three dimensions, it is not possible to increase the number of bits per second that they can carry. For simple on/off signaling, the transmission capacity of an electrical line can be written approximately as:

$$B \leqslant B_0 \frac{A}{L_2} \tag{1}$$

Where A is the cross-sectional area of the wiring, L is the lenght and B0 is a constant ($\backsim 10^{16}$ bits per seconds).The dimensionless A/L^2 ratio is what makes the transmission capacity independent of the size of the system. In addition, the physics of electrical lines leads to many other problems for signal integrity, such as the "cross-talk" between adjacent lines through capacitive coupling and reflections in the trasmission line.The second problem related to electrical interconnection is power dissipation. The performance of modern integrated circuits is increasingly limited by power dissipation, wihch is also becoming ecologically significant [12]. There are many sources of power dissipation in information processing. Basically, every logical operation must consume energy, and, in addition to these operations, there are other dissipations coming from leakage and subtreshold currents. For every unit of energy spent with logical operations, there will be a multiplier factor due to the power supply and to the sinking of thermal dissipation. However, the dominant contribution to the energy consumption can be attributed to the electrical interconnections, and this energy is associated to the charging and discharging the transmission lines[13]. In electrical communication, the whole line has to be charged up to at least the signaling

voltage, with an energy consumption:

$$E_s \leqslant C_l V_l^2 \tag{2}$$

Where C_l is the line capacitance and V_r is the signaling voltage. The capacitance of a typical line is around 2pF/cm, and since it is low sentitive to scaling, the only way to reduce the energy consumption is the reduction of the signaling voltage.

Optical Interconnects

Optical interconnects offer many advantages with respect to electrical interconnects, in particular regarding signal timinig and integrity. Optical channels are characterized by low dispersion, allowing the transimission of pulses through long distance without significant broadening, and the propagation velocity have a reduced temperature dependence. Wavelength division multiplexing increases the transmission capacity of a single channel. The "cross-talking" is not dependent on the bit rate, since it is much lower with respect to the carrier frequency, and physical phenomena such as signal reflection are much easier to be minimized. Optics has already replaced electrical wiring in long distance communications, and, as mentioned before, also in board-to-board commnications for some very important markets, however, interconnection density and power consumption are critical parameters to be considered in order to move the optical interconnect technology to shorter distance, such as on-chip applications. Optics does not have resistive losses in the transmission line, meaning that the bit rate is not limited by a relation such as the one expressed in equation 1.1 for electrical wiring. For this reason, optics is particularly attractive for long lines with limited cross sections. Regarding the power consumption, optics have an important advantage since it uses quantum sourcing and detection of the signal, whitout any need of line charging. The relevant energy is the one required to discharge the capacitance C_d of the photodetector and the electrical input to

which it is connected by the signal voltage:

$$E_p \geqslant C_d V_r \frac{\hbar\omega}{e} \tag{3}$$

where the voltage $\hbar\omega$ is equal to the photon energy in eV. Let's now examine in some detail the energy targets for optics. In order to be competitive with near future electric interconnections, the system energy per bit should be $\ll$ 50-200 fJ/bit, and even lower to meet demands out to 2022 according to ITRS projections. An optical system requires a transmitter driver circuit, an optical output device, an optical channel and a photodetector, with the relative circuit.

Receiver circuit

By considering a photodetector integrated with a transistor, we have to estimate the total capacitance given by the photodetector capacitance and the one of the transistor's gate. A photodetector with an area of a few square micrometers with a thickness around 100 nm should have capacitances of a few fF. On the other hand, the gate capacitance of an NMOS transistor is 1.2 fF/μm for the 32 nm node. Ge-on-Si photodetectors with the required capacitance have already been demonstrated [14],[15]. The total involved energy for such a system is in the femtojoules range.

Transmitter Circuit

The target energy for the transmission circuit is around 2-10 fJ/bit, as discussed in [9]. We can consider a transmitter circuit as a system involving a light source and a modulator. Up to now, a state-of -the-art laser has an energy consumption of 5.5 fJ/bit [6]. This laser is made of III-V semiconductors, and there is a general problem regarding the growth of III-V materials on silicon due to the lattice mismatch, which leads to crystal defects. Such defects are known to be detrimental for the device performance. III-V lasers can be bonded on silicon through evanescent coupling between the laser and the silicon waveguide, but such a complicated fabrication process is not suitable for large integration. The

preferred solution for on-chip application is the developement of a light source based on group IV elements. As mentioned before, Ge-on-Si laser have been demonstrated in electrically pumped configuration, however the performances of such device are still far from what required, not only in terms of energy consumption. Also off-chip laser sources have been considered. Even if there is a problem related to the coupling of light source to the chip, there are also several advantages such as the removal of additional power dissipation from the chip, and the possibility to optimize the laser performances without considering all the integration problems. For modulators, we have two broad categories, refractive and absorptive. Refractive modulators are limited by the absence of an high speed physical effect capable to give refractive index variations higher than 10^{-3}. With such a small variation, considering a Mach-Zendher modulator, device lenght of hundreds of micrometers are required in order to obtain a π phase shift, leading to energy consumptions in the range of hundreds of fJ/bit or higher. In order to have compact refractive modulators, the use of resonators or slow light is required. However it has to be considered that the tuning of such devices are obtained by thermal power, thus increasing the overall power consumption. Modulators based on electroabsorption works by changing the absorption spectrum of a semiconductor by appying an electric field to it. The two physical effects behind electroabsorption are the Franz-Keldysh (FK) effect for bulk semiconductors and the quantum confined Stark effect (QCSE) for quantum confined structures such as quantum wells. Both effects require electric fields in the range of 1-10 V/μm, easily obtainable in a reverse biased p-i-n structure in which the intrinsic region is made by the bulk or quantum well materials. These effects are able to enhance the optical absorption below the bandgap energy, in particular the FK effect is charachterized by a long and smooth absorption tail, with absorption coefficients in the range of some hundred cm^{-1}. Devices based on the FK effect tipically require a long interaction lenght. QCSE gives more abrupt spectral features, with typical absorption coeffient of several thousands cm^{-1}. The QCSE is a very strong physical effect, thus the realization of modulators with a lenght of a few micrometers is feasible.

Moreover, the QCSE modulators are expected to work at very high data rate, since it has been theorized that the fundamental speed limit of this effect is below the picosecond[17].In these devices the energy consumption is the energy required to charge up the active volume to the operative voltage. Devices with energies of a few tens of femtojoules have already been demonstrated[18].

Silicon Photonics

In this section the operation principles and state of the art silicon photonics devices is presented. For the pourposes of this thesis, the review will be focused on light sources and modulators. The first two subsections are dedicated to silicon, while the third one is focused on germanium based devices.

Silicon based light sources

Si and Ge are indirect bandgap semiconductors. Free electrons tend to stay in the lower valleys of the conduction band (X for Si and L for Ge) which are not aligned in the reciprocal space with free holes in the valence band. Radiative recombination can occur only if a third particle, a phonon, is ivolved in order to fulfill the momentum conservation, thus leading to slow optical transition rates. Two important non-radiative recombination processes are the Auger recombination and the free carrier absorption (FCA). Auger recombination is a three particle process in which an electron or an hole is raised to an higher energy level by absorbing the energy relased by an electron- hole recombination. The rate is proportional to the free carrier density and inversely proportional to the bandgap. In FCA an electron or an hole can be raised to higher energy levels by directly absorbing a photon. Also FCA is proportional to the carrier density, and in majority carriers devices such as lasers, or in heavily doped materials, it is usually higher than the material gain. For both these processes, the excited carriers relax the excess energy by emitting phonons and they have lifetimes much shorter with respect to radiative recombination.

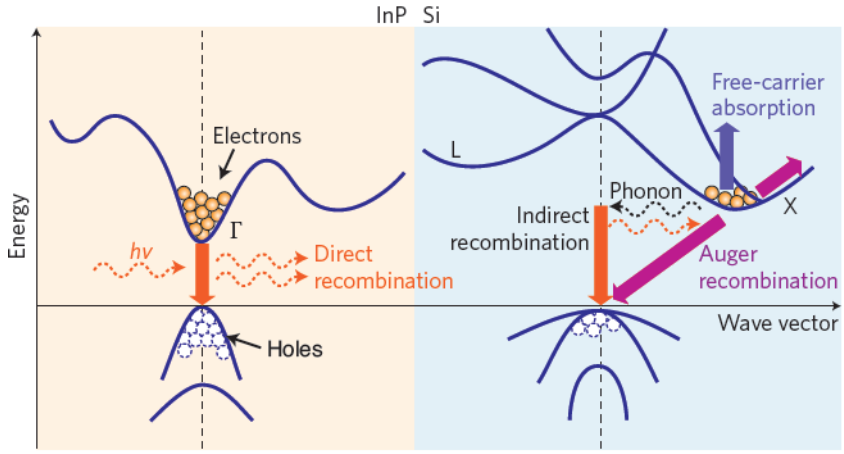

Figure 2: Scheme of the energy band diagram and major carrier transition process in Si and InP. Reproduced from [19].

Silicon Raman laser

The Raman effect is based on the inelastic scattering of a photon by an optical phonon. When a photon is absorbed by an atom at a certain vibrational state, it is raised to an intermediate higher state. The excess energy is usually released by the emission of a photon with the same energy, bringing back the system to the ground state, but it is also possible to see weak additional components with lower and higher energies with respect to the incident photon. These components are due to the absorption or emission of optical phonons, namely the Stokes and anti-Stokes transitions. Stimulated Raman scattering occurs when the medium is irradiated symultaneously with a pump beam and a signal beam which is resonant with the Stokes transition. A pulsed silicon Raman laser was demonstrated for the first time in 2004[21] followed one year later by the demonstration of continuous wave operation[22].Up to now, state of the art Si Raman lasers have a threshold power of 20 mW with an output power of 50 mW, with a spectal purity well beyond best the performance of laser diodes.

Integration of III-V lasers on Si

Another interesting approach in order to realize a silicon compatible light source is based on the growth of III-V materials such as GaAs or InP on silicon. It is very well known that the lattice and thermal expansion coefficient mismatches between these materials and silicon lead to an high density of threading dislocations (TD) (10^8-10^{10} cm^{-2}) in the grown material. Numerous approaches have been proposed in order to reduce the TD density, such as special surface treatement[23] and strained superlattices [24]. Recently SiGe buffer layers[25] have been used to realize GaAs based continuous wave lasers on silicon at room temperatures, but their reliability is still a problem for applications.

Hybrid silicon lasers

A promising approach, already employed in off-chip optical interconnection devices, is based on the bonding of III-V semiconductors on an silicon-on-insulator(SOI) substrate. In this way it is possible to combine very high quality materials with the lattice mismatch silicon substrate. Silicon passive optical circuits are processed before the transfer, and the III-V structures are fabricated after the transfer by standard optical litography. The first demonstration of an hybrid Fabry-Perot laser was done in 2006[26], followed in the last years by an optimization of the device architectures, leading to the realization of lasers with very high performances with treshold currents in the range of mA and mW output powers[27].

Silicon modulators

The physical effects traditionally employed in semiconductors to obtain electro-refraction (ER) or electro-absorption (EA) are the Pockels effect, the Kerr effect and the FK effect. Unfortunately these effects are very weak in pure silicon at the telecommunications wavelengths[28], thus alternative methods are required. One possibilty, since silicon has a very large thermo-optic coefficient, is to exploit the thermo-refractive effect. However it is not suitable for high speed

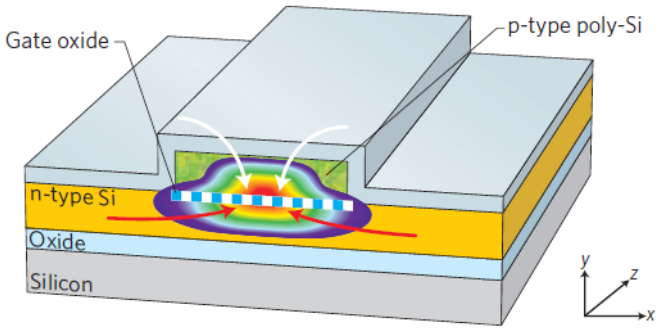

Figure 3: Cross section of the first high speed silicon modulator. Reproduced from [30].

applications. The most common effect in order to obtain modulation in silicon is the plasma dispersion effect. By changing the carrier density in the material, it is possible to change both the refractive index and the absorption coefficient at a given wavelength. The charge density can be changed electrically by injection, accumulation or depletion. The first breakthrough in silicon modulation technology came in 2004, when the first high speed modulator was demonstrated[29]. The device, capable of operating speed up to 1GHz, works by the accumulation of free carriers on the two sides of a dieletric layer inside a waveguide(See fig.3). The performances of carrier accumulation based modulators were later optimized. Recently Lightwire reported a modulator with an operating speed up to 10 Gbit/s at an extinction ratio[1] of 9dB, with an active lenght of 480μm[31]. Another technique based on the manipulation of the carrier density is the carrier depletion, in which the light beam propagates through the junction of a reverse biased p-n structure. This technique is particularly suitable for high speed operation, at the expense of the extinction ratio. Liu et al[32] reported transmission rate up to 40 Gbit/s in a device operating in

[1]extinction ratio is defined as the ratio of I_{max}, the intensity transmitted when the modulator is adjusted for maximum transmission, to I_{min}, the intensity transmitted when the modulator is adjusted for minimum transmission.It is quoted in decibels and expressed as $10log(I_{max}/I_{min})$

carrier depletion mode. Devices based on carrier accumulation or depletion are typically used in a Mach-Zehnder interferometer with a device lenght of hudreds of micrometers or even millimiters, thus the power consumption, which is in the range of hundreds of fJ/bit, is still to high for on-chip applications. A possible strategy in order to reduce the device footprint is the use of resonant structures such as ring resonators, which were introduced by Xu[33]. The device, based on carrier injection in a p-i-n structure, had a data rate of 1.5 Gbit/s. Further improvement moved the data rate up to 16 Gbit/s with an extinction ratio of 8dB. The ring diameter was only 12 μm, giving a footprint smaller than any Mach-Zehnder modulator. Mach-Zehnder interferometers with a reduced lenght were also fabricated by using photonic crystals[34]. Both ring resonators and photonic crystals are very effective in reducing the device footprint and the energy consumption while keeping high performances in terms of extinction ratio and data rate. However they suffer of a strong temperature dependence and very narrow working spectrum.

The role of germanium

It has been envisioned that germanium, thanks to its photonic properties and its compatibility with CMOS technology, will open the path through on-chip applications of silicon photonics. Ge and Si have significant mismathces both in lattice parameter and in thermal expansion coefficient, nevertheless the heteroepitaxial growth of Ge on Si has undergone a remarkable developement in the last decade. Nowadays, high quality Ge crystals grown on Si can be obtained with several growth techniques, including Chemical Vapor Deposition (CVD), molecular beam epitaxy (MBE) and low energy plasma enhanced CVD (LEPECVD). Initially, the interest in germanium for silicon photonics appication was driven by the possibilty to exploit the direct gap absorption to realize compact and efficient monolithic photodetectors on Si. The absortpion edge of Ge is located at 0.8 eV, thus both the 1.3μm and the 1.55 μm optical fibers windows can be covered by this material. Photodetectors with performances comparable

to III-V semiconductors have already been demonstrated both in p-i-n[35] and avalanche[36] configurations.

Ge based light sources

Despite its indirect band structure, germanium can be turned into an efficient light emitter by using heavy n-type doping and tensile strain, as theorized by Liu et al. [37].N- type doping is able to fill the L valley with electrons coming from the impurities, enhancing the efficiency of carrier injection into the Γ valley under external pumping [38] (See fig 4). On the other hand tensile strain is able to reduce the band gap and the energy separation between the direct and the indirect conduction band minima. The effect of tensile strain on the photoluminescence of germanium was experimentally demonstrated by Cheng. et al [39]. The authors used induced a biaxial tensile strain up to 0.36% by an external mechanical stressor and they observed a remarkable enhancement of the direct-gap related radiative recombination as the tensile strain was increased(See fig 5). The first demonstration of direct-gap related electrolumines-

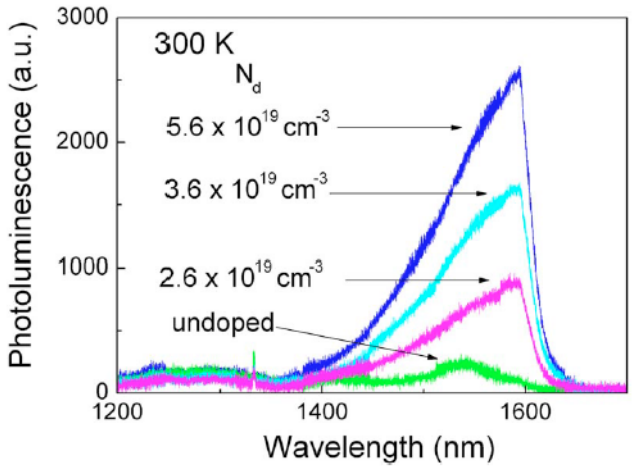

Figure 4: Room temperature photoluminescence spectra of phosphorous doped germanium [38].

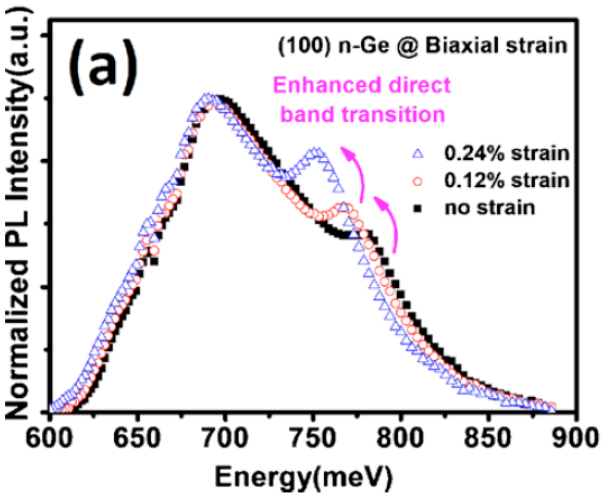

Figure 5: Room temperature photoluminescence spectra of tensile strained germanium [39].

cence was demonstrated in 2009 by Sun et al.[40]. In this work, a Si-Ge-Si p-i-n light emitting diode was fabricated and light emission at 0.77 eV was reported. The first demonstration of laser operation in Ge-on-Si was done in 2010 by the MIT group[7]. In their work, the authors exploited n-type doping and tensile strain to achieve lasing in an optically pumped Ge on Si waveguide. Two years later, the same group realized the first Ge on Si electrically pumped laser[8].In this work, the n-type doping was increased in order to achieve an higher gain, thus compensating for the additional losses caused by the electrical pumping. However, the laser have a very high current density treshold of 290 kA/cm^{-2}, which is very far from what required for silicon photonics applications.

Ge based modulators

Germanium exhibit a strong FK effect, that can be used to realize compact and efficient intensity modulators. Recently a SiGe FK modulator with a device lenght of only 50μm was demonstrated[41]. The device shows an extinction

ratio of 7 dB and a modulation speed up to 1 GHz. Thanks to the small device lenght, the energy consumption was as low as 50 fJ/bit. The breakthrough in germanium modulators technology came in 2005 with the first demonstration that a QCSE as strong as in III-V materials was achievable in Ge/SiGe MQW [42] (See fig 6). The sample, grown by reduced pressure CVD, was processed into a vertical illuminated p-i-n diode, with an intrinsic region constituted by ten periods of 10 nm Ge wells and 16 nm $Si_{0.15}Ge_{0.85}$ barriers grown on a relaxed $Si_{0.1}Ge_{0.9}$ buffer layer. After the first demonstration, many efforts have been made in order to study the structural and optical properties of Ge/$Si_{0.15}Ge_{0.85}$ MQW and to realize efficient optical modulators. In 2006, Kuo et al.[43] have demonstrated that this material system can be used to modulate light at the telecommunication wavelength of 1.55 μm. The quantum confinement and the compressive strain in Ge wells shift the direct-gap absorption edge of Ge from 0.8 eV (1.55 μm) to 0.88 eV (1.4 μm). The authors have demonstrated that the absorption edge can be shifted back to the C-band range by heating the device to 90^{o}C. Optical transitions in Ge/$Si_{0.15}Ge_{0.85}$ MQW were thoretically

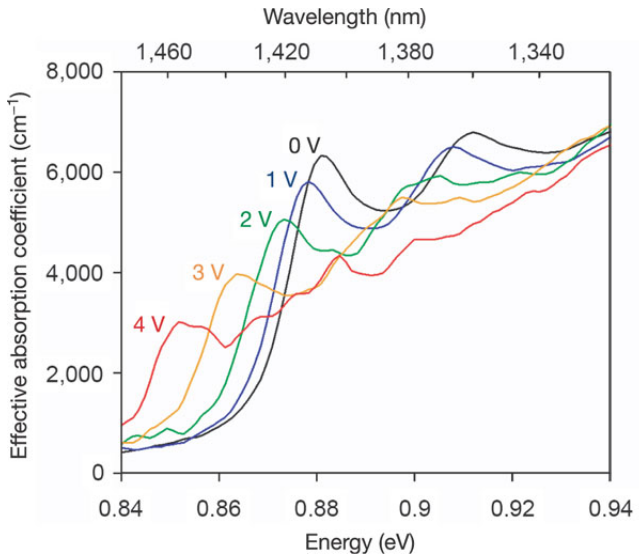

Figure 6: First demonstration of QCSE in Ge QW [42].

investigated by tight-binding[44] and by 8-band k.p [45]. Also the polarization dependence of the absorption spectra was theoretically [46] and experimentally [47] investigated. In [47] Chaisakul et al. compared the QCSE from the first two excitonic transitions (HH1-cΓ1 and LH1- cΓ1) as a function of light polarization by photocurrent measurements performed on planar waveguides. They observed that for an incident light with TE polarization both the HH1-cΓ1 and LH1- cΓ1 transitions are present, while for an incident light with TM polarization only the LH1- cΓ1 absorption peak is visible. Despite the higher optical losses at lower wavelength, the LH1- cΓ1 transition is more efficient by a factor 3 with respect to the HH1- cΓ1 transition for intensity modulation [48]. High speed and low power consumption in a waveguide integrated electro-absorption modulator was also recently demonstrated [18]. In this work the authors reported 23 GHz modulation speed with a power consumption of only 15 fJ/bit from a 3μm wide 90μm long Ge/SiGe waveguide. Ge/SiGe MQW are nowadays cosidered very promising in order to realize high performance silicon compatible modulators, expecially because of their extremely low power consumption.

Chapter 1

Germanium Bandstructure Engineering

1.1 Germanium Bandstructure

Germanium is a group IV element with a diamond lattice structure, characterized by the tetragonal coordination of each atom with its near-neighbours of the same unit cell. The valence band, which is originated by a linear combination of p-type orbitals, consists of three distinct bands: the heavy holes (HH) band, the light holes (LH) band and the split-off (SO) band, which lies at lower energies because of the spin-orbit interaction. The HH and LH bands are degenerate at the Γ point, which is the top of the valence band. The conduction band of germanium is far more complicated, because it is originated from a composition of spherical s-type orbitals and from strongly directional p-type and d-type orbitals. The conduction band has four minima located in the L point at $k =< 111 >$, with an energy gap E_{gL}=0.66 eV and another minimum located at the Γ point with an energy gap $E_{g\Gamma}$=0.8 eV (See Fig. 1.1).The energy difference between the two minima is very small, only$\Delta E = 0.14eV$. The band structure of germanium can be engineered by using strain, heavy n-type

doping and quantum confinement. Tensile strain is able to reduce the bandgap, enhancing the optical absorption at a given wavelength, and also to diminish the energy difference between the Γ and L minima, eventually inducing the cross-over and making Ge a direct bandgap material. The incorporation of n-type dopants in germanium allows to fill the indirect conduction valleys, enhancing the carrier injection efficiency under external pumping. Heavy n-type doping causes also an increase of the Fermi level of Ge and consequently widens the bandgap (see fig. 1.2). Quantum confinement is a very powerful tool to design the band structure of Ge. The technology of Ge/SiGe multiple quantum wells has attracted a great interest for the realization intensity modulators and light emitting diodes for silicon photonics applications.

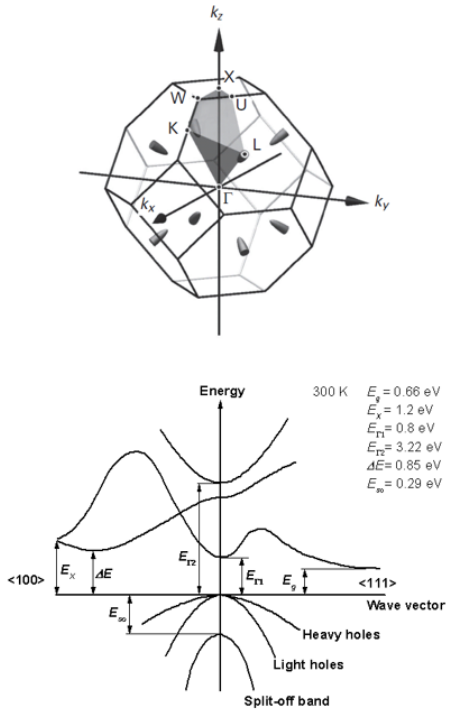

Figure 1.1: many valley structure (top) and band structure of Ge at 300K.

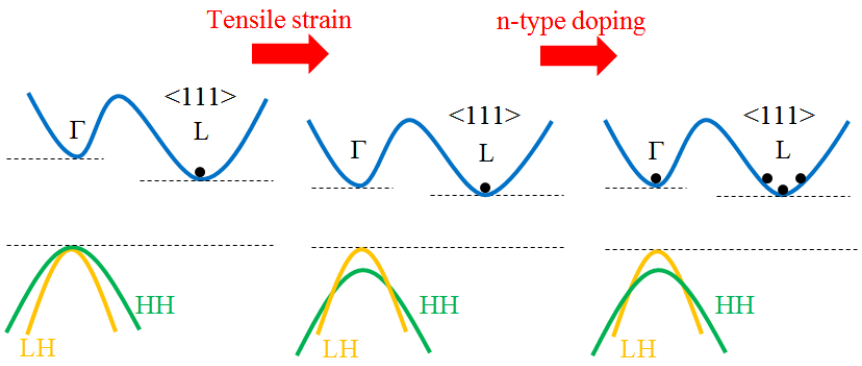

Figure 1.2: Schematic of the effect of tensile (biaxial) strain and n-type doping on the band structure of Ge.

1.2 Strain

Strain in crystals is created by deformation and it is defined as a relative lattice displacement. The strain state is expressed by a 3×3 matrix, the strain tensor:

$$\varepsilon = \begin{pmatrix} \varepsilon_{xx} & \varepsilon_{xy} & \varepsilon_{xz} \\ \varepsilon_{yx} & \varepsilon_{yy} & \varepsilon_{yz} \\ \varepsilon_{zx} & \varepsilon_{zy} & \varepsilon_{zz} \end{pmatrix} \tag{1.1}$$

Elastic strain in crystals is always the response to an applied stress, which can be expressed with the following 3×3 matrix, the stress tensor:

$$\sigma = \begin{pmatrix} \sigma_{xx} & \sigma_{xy} & \sigma_{xz} \\ \sigma_{yx} & \sigma_{yy} & \sigma_{yz} \\ \sigma_{zx} & \sigma_{zy} & \sigma_{zz} \end{pmatrix} \tag{1.2}$$

Stress and strain tensors both have only six independent components and they can be represented as a six elements column vectors. They are related through

the elastic compliance tensor:

$$S_{ij} = \begin{pmatrix} S_{11} & S_{12} & S_{13} & S_{14} & S_{15} & S_{16} \\ S_{21} & S_{22} & S_{23} & S_{24} & S_{25} & S_{26} \\ S_{31} & S_{32} & S_{33} & S_{34} & S_{35} & S_{36} \\ S_{41} & S_{42} & S_{43} & S_{44} & S_{45} & S_{46} \\ S_{51} & S_{52} & S_{53} & S_{54} & S_{55} & S_{56} \\ S_{61} & S_{62} & S_{63} & S_{64} & S_{65} & S_{66} \end{pmatrix} \tag{1.3}$$

In cubic crystals, for symmetry reasons, the elastic compliance tensor can be expressed by using only three independent constants. The complete equation that relates strain and stress in germanium is:

$$\begin{pmatrix} \varepsilon_{xx} \\ \varepsilon_{yy} \\ \varepsilon_{zz} \\ \varepsilon_{yz} \\ \varepsilon_{zx} \\ \varepsilon_{xy} \end{pmatrix} = \begin{pmatrix} S_{11} & S_{12} & S_{12} & 0 & 0 & 0 \\ S_{12} & S_{11} & S_{12} & 0 & 0 & 0 \\ S_{12} & S_{12} & S_{11} & 0 & 0 & 0 \\ 0 & 0 & 0 & S_{44} & 0 & 0 \\ 0 & 0 & 0 & 0 & S_{44} & 0 \\ 0 & 0 & 0 & 0 & 0 & S_{44} \end{pmatrix} \begin{pmatrix} \sigma_{xx} \\ \sigma_{yy} \\ \sigma_{zz} \\ \sigma_{yz} \\ \sigma_{zx} \\ \sigma_{xy} \end{pmatrix} \tag{1.4}$$

Any strain configuration can be computed by using the equation (2.4) if the stress tensor is known. In general the strain state of a crystal can be expressed as a superposition of an hydrostatic strain and of an uniaxial strain. This notation is very useful since the two kind of strain states have different effects on the band structure of the considered semiconductor. The hydrostatic strain is able to shift the average position of an energy band. It is responsible of the volume change of the crystal unit cell in response to the applied stress, and it can be expressed as the trace of the strain tensor. When two atoms are brought togheter to form a molecule, the interatomic interaction increases as they approach each other and, as a consequence, the bonding and anti-bonding energy levels become further apart in energy. Strain in crystals works in a similar way. Normally, when a compressive hydrostatic strain is applied to the crystal, the bandgap get wider. On the contrary, if the strain is tensile, the bandgap diminishes.The uniaxial strain might lift degeneracies of the energy

bands, depending on the relation between the strain direction and the position of the singular points in the bandstructure of the considered semiconductor. The average energy of the band is not affected by this strain component. A general stress will induce both hydrostatic and uniaxial strain, whose effects are schematically shown in fig. 1.3.

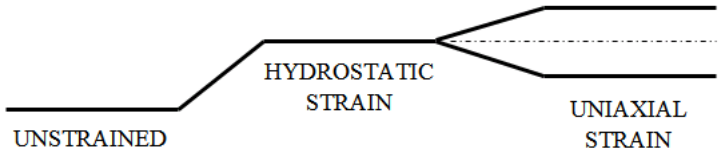

Figure 1.3: Schematic of the effect of hydrostatic and uniaxial strain on an energy band

1.2.1 Biaxial strain

Biaxial stress usually occurs in heteroepitaxial growth as a consequence of the mismatch of the lattice parameter or of the thermal expansion coefficient between the material constituting the substrate and the material deposited on it, which is forced to adapt its lattice parameter to that of the substrate, being in a state of elastic deformatin. The stress applied in the growth plane is able to induce a strain state which can be represented as a combination of hydrostatic strain and a uniaxial strain in the direction perpendicular to the growth plane. In this section, the effect of the biaxial strain for different planes on the band structure of Ge grown on Si will be discussed. All the simulations have been performed by using a NextNano, a code exploiting deformation potentials theory [51],[52]. The parameters used for the simulations are reported in Tab. 2.1. The band edges of Ge as function of the biaxial strain in the (100), (111) and (110) planes are reported respectively in Fig. 1.4, 1.5 and 1.6. In all the three cases, the top of the valence band has a light hole character for tensile strain

S_{11}	S_{12}	S_{44}	Δ_0	$a_{c,\Gamma}$	a_v	Ξ_u	Ξ_d	b	d
9.8	-2.7	14.8	0.29	-8.24	-1.24	15.13	-6.58	-2.16	-5.3

Table 1.1: Main parameters used for the simulations. Elastic compliance constants S_{ij} are given in m^2/N,deformation potentials and the spin-orbit interaction are given in eV.

and a heavy hole character for compressive strain. If the stress is applied along the (100) plane, the L minima are degenerate because the uniaxial component of the strain field is symmetrical with respect to the [111] direction. As the strain increases, the Γ band edge shift toward lower energies with a rate of 103 meV for 1% strain, while the L band edge shifts downwards with a lower rate of 29 meV for 1% strain. Thus the energy difference between the Γ and L minima decreases with increasing tensile strain, and the cross-over is expected for $\varepsilon = 0.19\%$. If the stress is applied in the (111) plane, the L minima are splitted by the shear strain into a set of three-fold degenerate bands (L_2, L_3 and L_4) and one non degenerate band L_1. The Γ edge shifts to lower energies with a rate of 96 meV for 1% strain, The $L_{2,3,4}$ bands rises with increasing strain at a rate of 36 meV for 1% strain, while the L_1 band shifts downwards with a rate of 221 meV for 1% strain. Since the L_1 minimum always lies at lower energies with respect to Γ, Ge biaxially strained in the (111) plane never becomes a direct gap material. If the stress is applied in the (110) plane, the L minima are splitted into two sets of two-fold degenerate bands (L_2, L_3 and L_1, L_4). The Γ edge downshifts with increasing strain at a rate of 132 meV for 1% strain. The $L_{1,4}$ minima shift to lower energies at a lower rate of 124 meV for 1% strain, meaning that a cross-over is expected, but at much higher strain levels with respect to the (001) case.

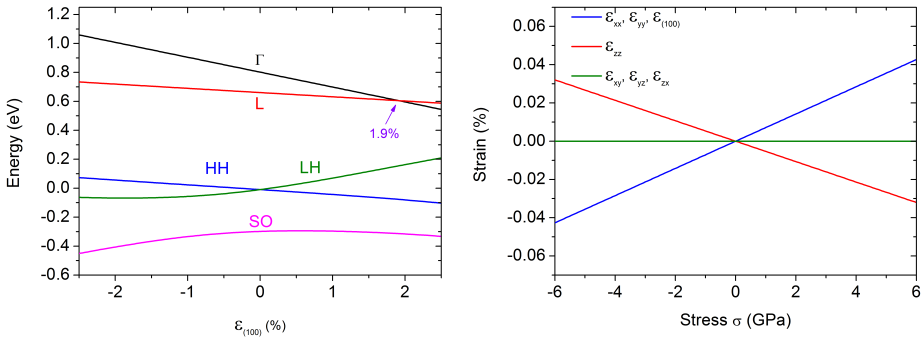

Figure 1.4: Band edges of Ge as a function of the strain (left) and components of the strain field as a function of the stress (right) for a biaxial stress in the (001) plane.

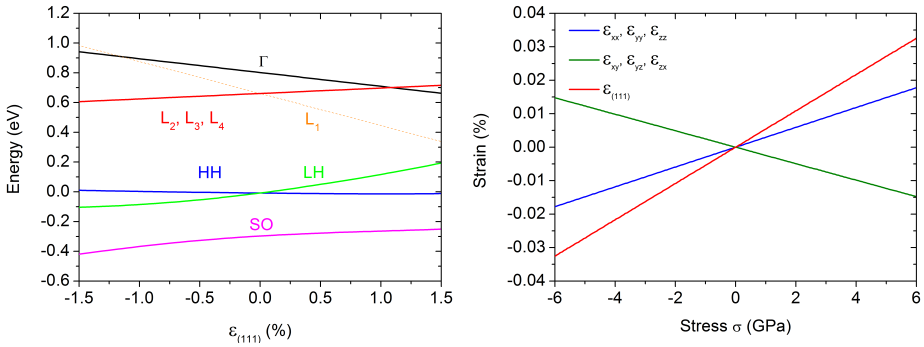

Figure 1.5: Band edges of Ge as a function of the strain (left) and components of the strain field as a function of the stress (right) for a biaxial stress in the (111) plane.

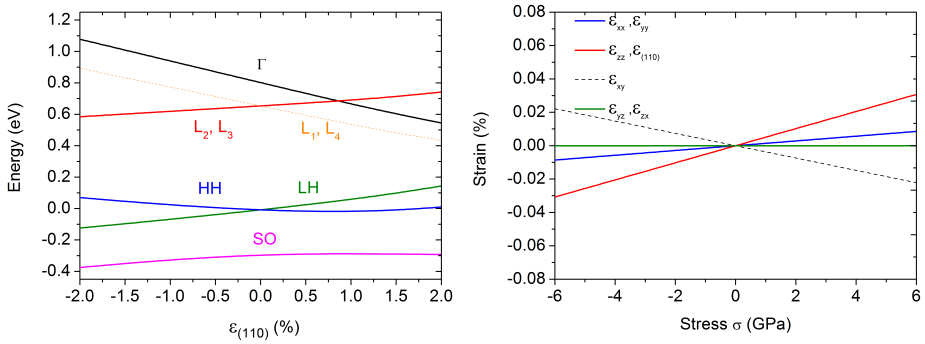

Figure 1.6: Band edges of Ge as a function of the strain (left) and components of the strain field as a function of the stress (right) for a biaxial stress in the (110) plane.

1.2.2 Origin of biaxial strain in Ge-on-Si technology

Lattice mismatch

Ge and Si have different lattice parameters. In particular, the one of Ge is 4.2% larger than the one of Si. During the heteroepitaxy, Ge initially adapt its lattice parameter to that of Si, being in a state of compressive biaxial strain and accumulating elastic energy. When a certain critical thickness is exceeded, the energy has to be relaxed plastically by the introduction of misfit dislocations. After the plastic relaxation the film recover its original lattice parameter. For highly mismatched material system like Ge and Si, the critical thickness is reached after a few nanometers. The situation is different if Ge is deposited on a Ge-rich SiGe layer. In this case the critical thickness is in the order of tens of nanometers. This is particularly important for the technonolgy of Ge/SiGe multiple quantum wells, where the strain state is a powerful tool to engineer the bandstructure. This topic will be discussed in detail in the next sections.

Thermal expansion coefficient mismatch

Normally the heteroepitaxial growth is performed at relatively high temperatures. In the case of Ge epitaxy on Si, the growth temperature is around 500^{o}C

but often, in order to get a better crystal quality, the growth is followed by thermal annealing cycles performed at very high temperatures (800^{o}C-900^{o}C). Since Ge has an higher thermal expansion coefficient (6×10^{-6} K^{-1}) with respect to Si (2.6×10^{-6} K^{-1}), during the cool-down process Ge tends to shrink faster than Si, and consequently it will be in a state of tensile biaxial strain, usually between 0.15%-025%. D.D. Cannon et al.[53] firstly observed this phenomenon. In ref. 53, a simple model has been proposed, which is mainly based on the maximum temperature reached during the annealing process. However, there is a rather large discrepancy in literature between the measured strain and what is expected by the aforementioned model. Capellini et al [54] studied the thermal induced tensile strain by means of a variable temperature high resoultion X-ray diffraction measurements. They observed that the tensile strain is partially compensated by the residual compressive strain due to the hardening limit of Ge, limiting the the maximum obtainable tensile strain to 0.25 %.

Post growth processing

Recently, many post growth processing approches have been proposed in order to obtain high level of biaxial strain in germanium film grown on silicon or on SOI substrates. El Kurdi et al.[55] have used a bulge/blister test appartus to mechanically induce a biaxial tensile strain (in the (001) plane) up to 0.6%in a germanium membrane. In the paper they reported a red-shift of 60 meV of the direct gap related photoluminescence (PL) peak at room temperature. Raja Jain et al.[56] have used a micromachining approach to induce an high level of biaxial strain in a germanium-on-insulator (GOI) layer. By using silicon nitride stressors, placed at the edges of a suspended GOI membrane, they have reported a biaxial tensile strain up to 0.82%. Capellini et al.[57] have used a CMOS compatible approach, involving silicon nitride stressors, to obtain a biaxial tensile strain in a Ge membrane deposited on a SOI substrate. They have reported strain levels up to 0.8%.

1.2.3 Uniaxial strain

Uniaxial stress can be applied to a crystal to induce a complex a strain field. It can be obtained externally, by mechanical stress, or by complex post growth processing. In this section, the effect of uniaxial stress applied in different crystallographic directions will be analysed and discussed. All the simulations have been performed by using the same NextNano code of the section 2.0.1, and the parameters used are reported in Tab. 2.1. The band edges of Ge as a function of the uniaxial strain in the [100], [111] and [110] directions and the respective strain fields in function of the applied stress are reported in Fig. 1.7, 1.8 and 1.9. In all the cases the valence band have a heavy hole character for tensile strain and a light hole character for compressive strain. If the stress is applied along the [100] direction, the resulting strain field has no shear components, and consequently the L minima are degenerate. The Γ minimum shifts downwards with increasing strain at a rate of 37 meV for 1% strain, while the L minima shift to lower energies at a lower rate of 10 meV for 1% strain. The cross-over is expected at a strain of 5.11 %.If the stress is applied along the [111] direction, then the strain field contains also shear components and the L minima are splitted into a three-fold degenerate set (L_2, L_3 and L_4), which rises in energy with increasing strain at a rate of 108 meV for 1% strain, and a single minimum L_1. The latter one downshifts at a rate of 54 meV for 1% strain. The Γ minimum shifts downwards at a lower rate of 33 meV for 1% strain, meaning that no crossover is expected if the stress is applied in the [111] direction. Finally, if the stress is applied in the [110] direction, the shear components of the strain field cause the splitting of L minima in two two-fold degenerate sets (L_1, L_4 and L_2, L_3). The first set rises in energy at a rate of 97 meV for 1% strain and the second set shifts downwards at a rate of 127 meV for 1% strain. The Γ minimum downshifts at a rate of 87 meV. Also in this case the crossover is not expected.

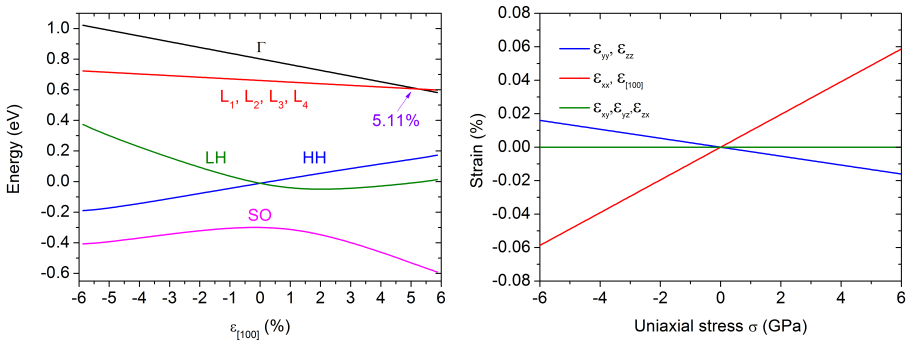

Figure 1.7: Band edges of Ge as a function of the strain (left) and components of the strain field as a function of the stress (right) for uniaxial stress in the [001] direction.

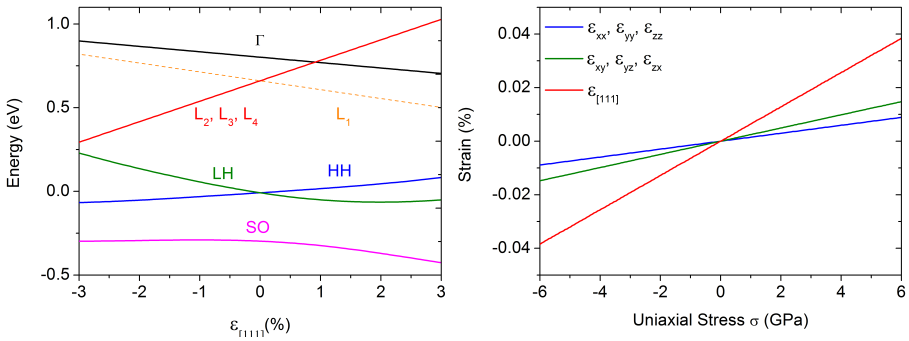

Figure 1.8: Band edges of Ge as a function of the strain (left) and components of the strain field as a function of the stress (right) for uniaxial stress in the [111] direction.

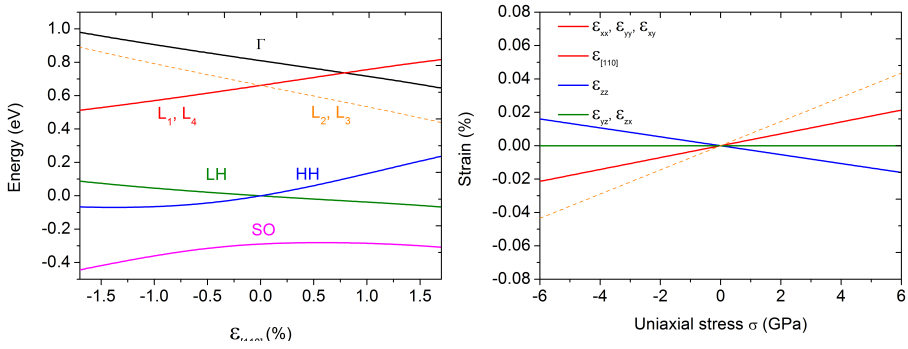

Figure 1.9: Band edges of Ge as a function of the strain (left) and components of the strain field as a function of the stress (right) for uniaxial stress in the [110] direction.

Origin of uniaxial strain in Ge-on-Si technology

Uniaxial strain in germanium can be obtained mainly by mechanical approaches or post-growth processing. Ghrib et al. fabricated Ge ridge waveguides stressed by silicon nitride layers, achieving a uniaxial tensile strain up to 1% in the [100] direction [58]. The method described in[56] has been used also to get an uniaxial tensile strain up to 1.5%.

1.3 N-type doping

In the previous section it has been shown that tensile strain is able to reduce the energy separation between the L and Γ valleys, eventually leading to a cross-over, with important consequences for the developement of Ge-on-Si laser sources. Unfortunately the strain levels required to achieve such a cross-over are very difficult to reach in practice. Another tool that can be used in combination with tensile strain in order to enhance the direct gap recombination is the n-type doping. By raising the Fermi level into the conduction band, heavy n-type doping is very effective in increasing the electron population in the Γ valley, thus reducing the carrier density necessary to satisfy the Bernard-Douraffourg

condition[59].The enhanced direct bandgap recombination has been recently observed in photoluminescence studies [38]. Unfortunately, the enhanced efficiency may be counterbalanced by an increase of nonradiative recombination as the doping level is increased. The Schockley-Read-Hall lifetime can be decreased by several order of magnitude as the doping is increased [60], thus decreasing the internal quantum efficiency. Another important drawback is related to the free-carrier absorption (FCA), which is linearly proportional to the electron or hole carrier density. FCA in n-doped germanium was studied in the 1960's [61][62][63]. Liu et al [37] fitted the data of Newmann and Spitzer for the modeling of optical gain. Carrol et al [64] studied the photoinduced FCA. They observed a strong FCA due to the valence intraband absorption, in particular between the heavy holes and the split-off bands.

1.3.1 Free carrier absorption

In highly doped germanium the losses are dominated by the FCA, usually described by:

$$\alpha_f(\lambda) = AN\lambda^a + BP\lambda^b \tag{1.5}$$

where A,B,a,b are constants, N and P are the electrons and holes density and λ is the wavelength. Liu et al. [37] obtained the following expression by fitting the FCA data in n^+Ge and p^+Ge:

$$\alpha_f(\lambda) = -3.4 \times 10^{-25} N\lambda^{2.25} - 3.2 \times 10^{-25} P\lambda^{2.43} \tag{1.6}$$

The authors reported that for 0.25% tensile strained Ge with a donor concentration of 7.6×10^{19} cm^{-3} the injection level required to overcome the FCA losses is 3.5×10^{18} cm^{-3}. Carrol et al. [64] studied the role of the valence intraband absorption in limiting the optical amplification for lasing. The authors carried out transmission and reflection spectroscopy in several Ge samples with different strain and doping levels, and they found out that, even in presence of a remarkable direct-gap gain, the corresponding photoinduced valence intraband absorption (PIA) losses are too high to obtain optical amplification. The PIA

absorption can be modeled by the follwing expression:

$$\alpha_{PIA}(E_{DG}) = \sigma_e N_e + \sigma_h N_h \tag{1.7}$$

where $\sigma_h = 3.8 \pm 0.2 \times 10^{-3} nm^2$ and $\sigma_h/\sigma_e = 12 \pm 1$. The SO-HH transition is likely the dominant source of PIA near E_{DG} because of the energy offset and the relative HH and SO effective masses.

1.4 Quantum Confinement

In recent years an increasing interest has been devoted to the study of coherently strained SiGe/Si and SiGe/Ge heterostructures. In particular, Ge-rich SiGe heterostructures have been widely investigated because their optical properties are expected to exhibit close analogies to those of direct gap semiconductors thanks to the proximity of the direct Γ and indirect L gaps. Early attempts to study the optical properties of this material systems have been performed by Taguchy et al. [65] on SiGe/Ge heterostructures grown on Ge and by Miyake et al. [66] on SiGe/Si heterostructures grown on Si. If we consider a $Si_{1-x}Ge_x$ layer pseudomorphically grown on a $Si_{1-y}Ge_y$ virtual substrates, according to the values of x and y concentration and on the growth direction, a variety of different band structures can be obtained. In particular, the problem of defining for a given set of concentrations (x, y) the corresponding band alignment soon emerged as a central item in the theoretical and experimental study of Si/Ge devices. Virgilio and Grosso [67] have demonstrated that if $y > 0.7$ and $x > 0.75$ the band alignement is of type I, leading to the formation of a quantum well for both electrons and holes. In Fig. 2.11 the typical absorption spectra of a bulk material and of a quantum well area shown. The quantum confinement leads to a step-like absorption spectrum, which result in a sharper edge with respect to the bulk material. Additionally, the quantum confinement increases the binding energy of excitons, resulting in clear excitonic resonances at room temperature, which are able to enhance the absorption contrast. When an electric field is applied perpendicular to the quantum well plane, the potential profile is tilted, and the

bandgap is decreased, thus leading to a redshift of the absorption spectrum. Moreover, the electric field is able to pull electrons and holes at the opposite side of the quantum well, reducing the exciton binding energy and the corresponding absorption peak. This phenomenon is called quantum confined stark effect (QCSE). The QCSE is one of the strongest physical phenomena to obtain optical modulation, it was observed for the first time in GaAs/AlGaAs MQW [68]. As a breakthrough, Kuo et al. [42] in 2005 discovered a strong QCSE in $Ge/Si_{0.15}Ge_{0.85}$ MQW, opening a new way to integrate high performance modulators on silicon.

1.4.1 Quantum Confined Stark Effect

The electric field dependence of the optical absorption near the band edge in semiconductor is an extensively studied subject. In bulk semiconductors, the resultant shift and broadening of the band edge absorption is known as Franz-Keldysh effect. At low temperature, the absorption edge, expecially in direct gap semiconductors, is dominated by the exciton resonance. When an electric field is applied, the resonance is able to shift for only the 10 % of the exciton binding energy before the broadening becomes so strong that the peak become

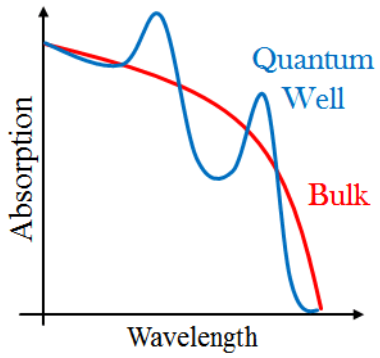

Figure 1.10: schematic absorption spectra of a bulk semiconductor and of a quantum well

unresolavble. On the other hand, if the electric field is applied to a quantum well, there are two major differences with respect to the bulk case: the large shifts obtainable and the persistance of the exciton peaks at large electric fields (even 50 times the exciton binding energy)(see fig. 1.10). D.A.B. Miller et al [68] proposed the following mechanism to explain these differences. The electric fields perpendicular to the quantum well layers pull the electrons and holes at the opposite sites of the well, thus reducing the energy of the electron-hole pair. This phenomenon causes the large red-shift and the reduction of the absorption peaks. The persistance of the resonances is explained by two separate reasons: (i) the walls of the QW impede the carriers from tunneling out of the well, and (ii) since the well width is usually smaller than the exciton radius, the electron-hole interaction, even if slightly weakened, remains strong enough to ensure the presence of well defined excitonic states. The effects of the QCSE on the band structure and on the absorption spectrum of a QW are schematically represented in fig. 1.11.

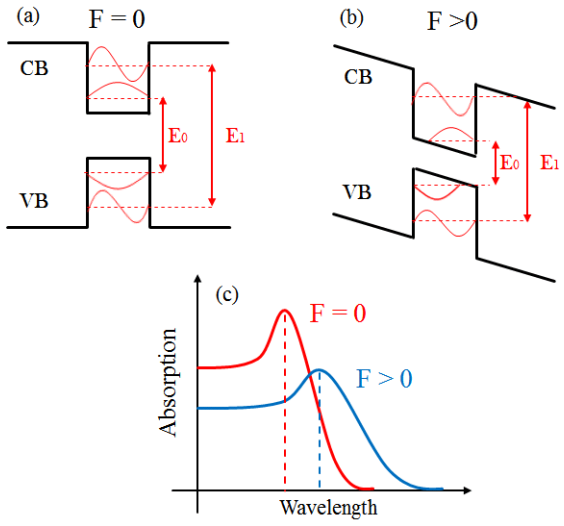

Figure 1.11: Schematic of the effect of the QCSE on the band structure of a quantum well (a)(b) and on the absorption spectrum (c)

Chapter 2

Heteroepitaxial growth of SiGe alloys

2.1 Introduction

Epitaxy refers to the deposition of a crystalline epilayer on a crystalline substrate. The word *epitaxy* comes from the Greek words epi, meaning "above", and taxis, which means "in an ordered manner". In the heteroepitaxial growth, the epilayer and the substrate are made by different materials, characterized by different lattice parameters and thermal expansion coefficients. As discussed in the previous chapter, strain is a very important element to be considered in heteroepitaxy. In this chapter, the main technological challenges related to heteroepitaxy of highly mismatched material systems such as Ge and Si are analyzed and discussed.

2.2 LEPECVD

Low temperature deposition techniques have attracted an increasing interest in semiconductor technology for the possibility to obtain extremely sharp doping

profiles and to exploit the kinetical suppression of three-dimensional growth in heteroepitaxy. Silicon-germanium with a very high crystalline quality have been obtained by chemical vapor deposition (CVD) and by molecular beam epitaxy (MBE). MBE offers a precise control on layer thicknesses and interfaces and allows extremely sharp doping transition between doped and undoped regions. However this growth tecnhinque find its main limitation in the very low growth rates. CVD processes are generally preferred and would most probably be the solution chosen for industrial application of Ge based devices. In typical CVD, the substrate is heated and exposed to one or more volatile precursors, which are thermically decomposed close to the substrate surface. UHV-CVD(Ultra High Vacuum CVD), LPCVD (Low Pressure CVD) or RPCVD (Reduced Pressure CVD), just to give a few examples, have already been used to grow high quality Ge-on-Si. The main drawback of CVD-based technique is that the growth rate is strongly temperature dependent, and for Ge it become unacceptably low for substrate temperature below 600 C. To overcome this problem, the energy required to decompose the precursors in the growth chamber must be provided in a non-thermal way. Plasma enhancement has been recognized long ago as a possible solution, but the energy of the ions must be controlled to avoid damages to the epilayers. This is the rationale behind low energy plasma enhanced chemical vapor deposition (LEPECVD). In a LEPECVD reactor, the wafer is exposed to an high intensity plasma, leading to growth rates of several nm/s through a very efficient decomposition of the reactive molecules. Since the plasma is obtained by a low-voltage DC arc discharge, the ions energies are in the range of tens of eV, low enough to allow the growth of crystalline materials. In a LEPECVD reactor, the plasma is generated by a Balzers ULS400 plasma source into which the discharge gas, Ar, is fed directly. The plasma source contains a Ta filament heated by a direct current of 130 A.The plasma is ignited by applying a relatively low voltage of 20-30 V between the grounded chamber walls and the hot filament. The source is connected to a UHV chamber through a 1 cm wide orifice. Its geometry is defined by a grounded anode in the lower part of the growth chamber and by a magnetic field, induced by a combination of

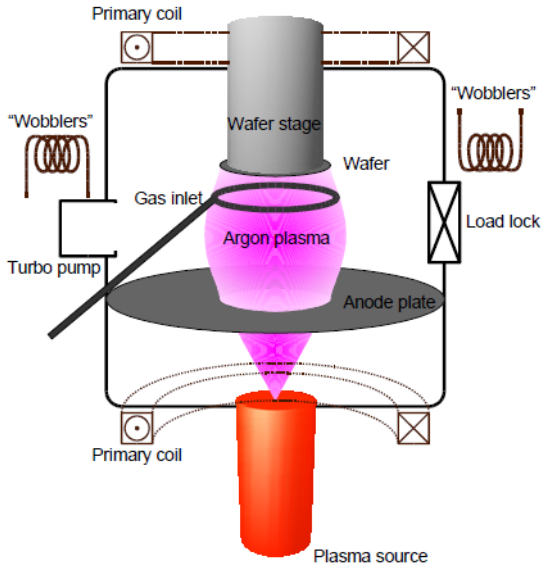

Figure 2.1: Schematic of a LEPECVD reactor.

coils and permanent magnets. The reactive gases, SiH_4 , GeH_4 ,B_2H_6 and PH_3 ,are fed into the growth chamber through a gas dispersal ring placed above the anode. The gas flows are regulated by mass flow controllers, having a maximum flux of 25 sccm for SiH_4 and GeH_4 and 10 sccm for B_2H_6 and PH_3. The dopant gases are diluited in Ar respectively 1% and 5%. Penumatic valves are used to switch the gas lines with a minimum interval of 1s. The substrate is kept at a fixed potential with respect to ground by means of an external power supply. The substrate temperature is adjusted between 200C and 750C by radiation heating from a boron-nitride coated graphite heater, which is regulated by a standard thermocouple and a PID controller. The deposition chamber has a base pressure of 10^{-9} mbar, while the working pressure is much higher reaching 10^{-2} mbar. The pumping system consists in a primary turbomolecular pump followed by a pre-vacuum stage (rotary pump). A scheme of the reactor is shown in fig. 2.1. The growth rate is mainly controlled by the plasma density and by the gas flows and it is almost independent from the substrate temperature.

For this reason, the growth rate and the surface diffusivity of the adatoms are completely decoupled, and they can be optimized separately. Moreover, since the decomposition of the reactive molecules is dominated by the plasma, the surface chemistry between the substrate and the reactive molecules plays a modest role on the determination of the alloy composition, which can be easily controlled by the gas flows.

2.3 Growth modes

The growth rates can be easily tuned from 0.1 $\AA$/s up to 10 nm/s, making LEPECVD an extremely versitile growth technique. The "high rate" growth mode is used to fastly deposit thick Ge or SiGe layers with high efficiency in the gas usage. The high rate settings features an arc current of 50A and a magnetic field of 10mT to efficiently confine the plasma in the substrate region. In order to deposit $Si_{1-x}Ge_x$ layers with x<(>)0.5, the SiH_4(GeH_4) flow is kept to the maximum value, while the GeH_4(SiH_4) is varied. The relationship between the alloy composition and the ratio of SiH_4 and GeH_4 is determined by performing HR-XRD measurements on five calibration samples. The "low rate" growth mode on the contrary is used when a precise control on the layer thickness is required. The reactor settings in this case features an arc current of 30A and a magnetic field of 1 mT, and the total gas flow is mantained at 5 sccm. There is also an "intermediate rate" used to deposit multilayered samples with a very high number of periods. The reactor settings for intermediate rate are the same as the low rate, but the maximum total gas flow in this case is 40 sccm. The standard growth temperature for pure Ge and pure Si are respectively 500C 740C. For SiGe layers the growth temperature is chosed by a linear interpolation. For multilayered structure the temperature is usually lowered to 450C to suppress the intermixing.

2.4 Strain related phenomena in heteroepitaxial growth

Heteroepitaxial growth is charactherized by the lattice mismatch between the material to be deposited, the so called epilayer, and the material constituting the substrate. The lattice mismatch for cubic crystal can be expressed as:

$$f = \frac{a_f - a_0}{a_f} \tag{2.1}$$

where a_f and a_0 are respectively the lattice parameters of the epilayer and of the substrate. The lattice mismatch causes an accumulation of elastic energy in the epilayer, described by:

$$E_e = 2\mu \frac{1+\nu}{1-\nu} \varepsilon^2 t \tag{2.2}$$

where μ is the shear modulus, ν is the Poisson coefficient, ε is the in-plane strain and t is the thickness. As the thickness increases, the accumulated energy can be relaxed in different ways. For the pourpose of this thesis, the discussion is focused on plastic relaxation by the introduction of misfit dislocations at the interface between the epilayer and the substrate. If the lattice parameter of the epilayer is larger with respect to that of the substrate, some atomic planes are terminated at the interface without continuation into the epilayer (See Fig. Such a defect is called dislocation. The dislocation is characterized by the direction l and the Burgers vector b. The plane $(b \times l)$ is called the glide plane. Dislocations can move within this since plane only small atomic displacements are necessary for gliding. The energy of a single dislocation is given by:

$$E_{ds} = A \left[ln \frac{r_a}{r_b} \right] \tag{2.3}$$

where r_a and r_i are respectively the inner and outer radius of the dislocation and A is defined as:

$$A = \frac{\mu b^2}{4\pi(1-\varepsilon)} \tag{2.4}$$

An orthogonal network of misfit dislocation has an areal energy:

$$E_d = \frac{2}{p} E_{ds} \tag{2.5}$$

The critical thickness can be found by calculating the force balance on a dislocation line, as proposed by Matthews and Blakeslee [69]. By following their procedure, it is possible to find the critical thickness h_c at which the first dislocations are introduced:

$$f = \frac{b}{h_c}\left(\frac{1-\varepsilon/4}{4\pi(1+\varepsilon)}\right)\left[ln\frac{h_c}{b}+1\right] \tag{2.6}$$

Another approach consists in equating the strain energy of the epilayer to the energy of a dense network of misfit dislocations spaced by apart by 4b. This approach was used by People and Bean [70] to find an alternative expression for the critical thickness:

$$f^2 = \frac{b}{32\pi h_c}\frac{1-\varepsilon}{1+\varepsilon}ln\frac{h_c}{b} \tag{2.7}$$

The model developed by People and Bean give a much larger critical thickness with respect to the previuos one. The critical thickness in this case is the thickness for which the epilayer is fully relaxed. As it can be seen in fig. 2.3, for pure germanium grown on silicon the critical thickness is of a few nanometers. Each misfit dislocation is terminated by two threading dislocations which penetrate through the epilayer at 60^o on the (111) plane (see Fig. 2.4). The typical density of threading dislocations for pure Ge grown on Si is 10^9-10^{10} cm^{-2}, which is significantly higher than what can be tolerated for any electronic or photonic

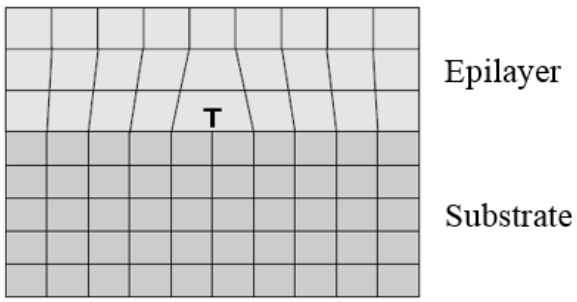

Figure 2.2: Strain relaxed epilayer with one misfit dislocation in the center. Reproduced from [50].

device. Threading dislocations are electrically active defects that can either trap or interact with electrons and holes, and the reduction of their density to acceptable values is one of the main challenge in the epitaxy of SiGe alloys on silicon.

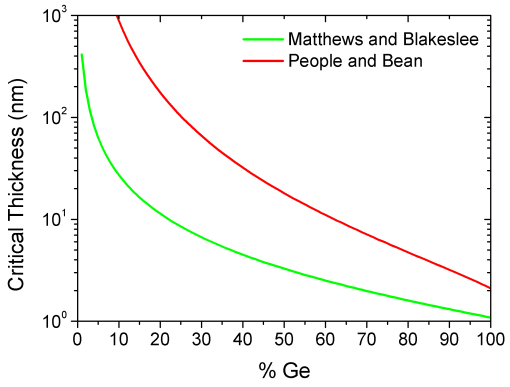

Figure 2.3: Critical thickness for a SiGe epilayer on a silicon substrate as a function of the Ge percentage in the alloy.

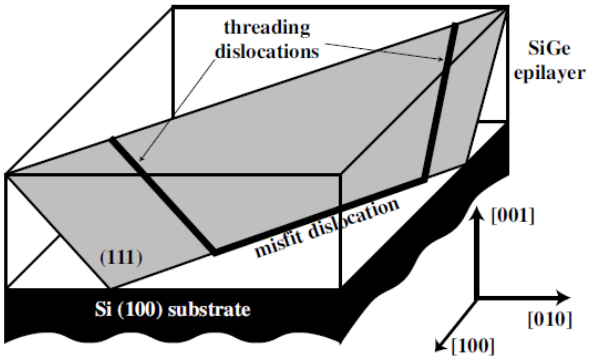

Figure 2.4: Schematic diagram of the relaxation of a SiGe epilayer by the introduction of a misfit dislocation with the two threading segments. Reproduced from [50].

2.5 Growth of pure Ge on Si

Usually the epitaxy of Ge on Si is performed in a two-step process. In the initial growth step, a thin Ge seed with a thickness of 30-60 nm is deposited at very low temperatures (320-360 ^{o}C) in order to supress the islanding due to the strain. Then the chamber temperature is raised to 600-650 ^{o}C to achieve higher growth rates and crystal quality. In a LEPECVD reactor this is not necessary because the islanding is kinetically suppressed. The whole deposition is performed in a single step at a temperature of 500^{o}C. After the growth, in order to reduce the threading dislocation density, thermal annealing cycles are performed between 800^{o}C and 600^{o}C. The thermal stress, which is produced by the change of temperature between the high and low temperature steps, generates a force, causing the dislocations to move. If two dislocations meet, they react and annhilate each other. The effectiveness of this procedure is strongly influenced by the thickness of the epilayer (see Fig. 2.5). As the thickness increases, the probability that two dislocations can meet and annhilate is strongly increased.

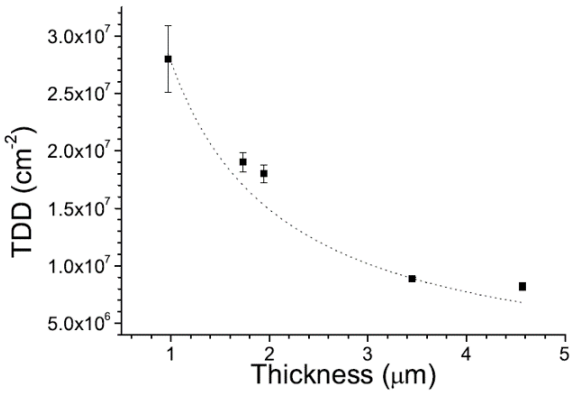

Figure 2.5: Experimentally measured threading dislocation density as a function of the epilayer thickness.

2.6 Deposition of Ge/SiGe MQW

From the technolgical point of view, the deposition of Ge-rich Ge/SiGe MQW is quite complicated. In order to obtain sharp interfaces between the Ge wells and the SiGe barrier, the growth is performed at low temperature, typically between 425^{o}C and 475^{o}C. The low growth temperature ensures a limited interdiffusion between the layers. Moreover the deposition is usually performed at low or intermediate rate to have a good control on the thickness. The to main problems, discussed in the next subsections, are the design of the virtual substrate and the strain compensation in the MQW stack.

2.6.1 Virtual substrates

The design and optimization of the virtual substrate is extremely important, because it influences significantly the structural and optical properties of the MQW stack. The Ge content in the virtual substrate (VS) sets the lattice parameter and the strain states for both the wells and the barriers. Moreover, since the VS is designed in order to have the same Ge content of the MQW stack, the threading dislocation density of the VS is replicated in the MQW stack. From the structural point of view, the main requirements are a low threading dislocation density, a smooth surface and the full relaxation of the VS. Also the thickness is an important design parameter. Considering that the Ge/SiGe structure is meant to be used as an optical modulator, a low thickness is preferred since it facilitates the integration with silicon waveguides. The simpest way to deposit a fully relaxed Ge-rich VS is to grow a SiGe layer directly on silicon, followed by some thermal annealing cycles in order to reduce the TDD. Unfortunately the annealing procedure is much less effective in SiGe than in Ge. Alloy disorder inhibits dislocation gliding, thus reducing the probability that threading dislocations can meet and annhilate. Moreover, the annealing procedure is known to enhance the surface roughness of SiGe layers. Nevertheless many efforts have been made in order to optimize the "simple" SiGe buffer layer because of the low thickness. Miller et al. [43] used a double

step deposition followed by annealing. The "simple" SiGe buffer can also be deposited on a patterned SOI substrate to obtain selective area growth. This technique was successfully employed with pure Ge grown on Si to reduce the TDD through the aspect ratio trapping [71], and recently it was extended to SiGe grown on SOI substrate by the group of Miller [72]. Another approach to obtain an high quality SiGe VS is the deposition of the so called "graded buffer". In a graded buffer, the Ge content is lineraly increased from 0% to the required value, with a low grading rate which is usually kept below 10%/μm, while the growth temperature is linearly decreased from 740 to 500 according to the alloy composition. This technique was firstly introduced by Luryi et al [73] and deeply studied by Fitzgerald [74]. By grading the concentration of Ge in the alloy, the strain of each epilayer is low, thus the threading dislocations coming from the initial layers can be used to relax the strain in the successive layers. The nucleation of new misfit dislocations is supressed by this mechanism, and thrading dislocation density as low as 10^{-6} cm^{-2} can be obtained for a final Ge concentration around 90%. The major drawback is that the final thickness of the buffer layer exceeds 10 μm, thus the graded buffer technique cannot be considered for CMOS integration. Another possibility is the deposition of a reverse graded buffer. In this approach, a pure Ge layer, usually 1μm thick is deposited and annealed, followed by the deposition of a SiGe layer with a Ge concentration linearly decreasing from 100% to the desired value. This technique was firstly proposed and studied by Shah [75]. The authors reported a TDDs comparable to those obtainable with the graded buffer technique, with a total thickness of the VS of only 2.8 μm. All the MQW samples described in this thesis were grown by the graded buffer technique.

2.6.2 Strain compensation in multilayers

For the growth of strained multilayers such as multiple quantum wells, the strain management is a critical point. In order to obtain a multilayered structure with an high crystal quality, two requirements have to be fulfilled. The thickness

of each single layer must be kept below the critical one (the lattice mismatch has to be calculated with respect to the VS) in order to avoid the nucleation of misfit dislocations at all the interfaces. For the same reason, the thickness and composition of every layer must be designed in order to perfectly compensate the tensile and compressive forces. In many cases it is sufficient to design a multilayer with the same average composition of the VS. In this case, the strain compensation condition can be expressed as:

$$\frac{h_a}{h_b} = \frac{G_b}{G_a}\left[\frac{a_b - a_a}{a_a\left(\frac{a_{VS}}{a_a} - 1\right)} - 1\right]. \tag{2.8}$$

For some technological applications it is useful to have a small compositional mismatch between the multilayer and the underliyng VS. For example, it is possible to generate a favourable discontinuity in the refractive index profile through the structure by increasing the average Ge content in the MQW region with respect to the VS. In this way it is possible to obtain an higher refractive index in the MQW region, thus increasing the overlap with the optical mode. Interestingly the crystal quality of the multilayer is not seriously affected by the absence of a perfect strain compensation.

Chapter 3

Ge/SiGe MQW for silicon photonics

3.1 Optical modulation at 1.3 μm

3.1.1 Introduction

Several optical fiber telecommunications systems work in the spectral window around 1.3μm, which corresponds to zero dispersion in standard single mode fibers. In particular some passive optical network architectures use 1.3μm radiation for upstream signal[76]. Therefore it is highly desirable to fabricate optical modulators operating at this wavelength. The first demonstration of modulation at 1.3μm by exploting QCSE in Ge/SiGe MQW was made by Lever et al.[77]by using Ge/$Si_{0.4}Ge_{0.6}$ MQW grown on a $Si_{0.22}Ge_{0.78}$ virtual substrate. With this material system, the large compressive strain in the wells pushes the HH1-cΓ1 transition at 1.3μm. In this section, our work on modulation at 1.3μm is presented. In order to fabricate a QCSE modulator operating at 1.3μm, we have used Ge/$Si_{0.35}Ge_{0.65}$ MQW grown on a $Si_{0.21}Ge_{0.79}$ virtual substrate. In this material system, the excitonic resonances are wider with respect to Ge/$Si_{0.15}Ge_{0.85}$ MQW because of the enhanced Γ-Δ scattering. This problem

will be analyzed and discussed.

3.1.2 Sample growth and charachterization

The sample was grown by LEPECVD on a 4 inch p-Si(001) substrate with a resistivity in the range of 1-10 Ωcm. Before the heteroepitaxial growth, the native oxide was removed by dipping the substrate in a hydrofluoric acid solution (HF:H2O 1:10) for 30 s. The first part of the structure is made by an 11 μm thick $Si_{1-y}Ge_y$ graded buffer, deposited at a rate of 5-10 nm/s, in which the Ge concentration y is linearly increased from 0% to 79% with a grading rate of 7%/μm. The top part of the graded buffer consists in a 2 μm $Si_{0.21}Ge_{0.79}$ layer forming a fully relaxed virtual substrate. A 500 nm boron-doped $Si_{0.21}Ge_{0.79}$ layer was deposited to form the p-type contact region, followed by a 50 nm thick $Si_{0.21}Ge_{0.79}$ spacer. The MQW structure is made of 20 periods of 8 nm thick Ge QWs and 12 nm thick $Si_{0.35}Ge_{0.65}$ barriers grown at 475C at a rate of 1 nm/s. Finally a 50 nm $Si_{0.21}Ge_{0.79}$ spacer and 200 nm phosphorus doped $Si_{0.21}Ge_{0.79}$ layer were deposited. A cross section of the structure is shown in fig. 3.1. Layer compositions, thicknesses and strain states were measured by high-resolution X-ray diffraction (HR-XRD) reciprocal space mapping (RSM) about the (004) and (224) reflections using a PANalytical X'Pert PRO MRD diffractometer. Out-of-plane and in-plane lattice parameters, $a_\perp$ and $a_\parallel$, were measured for the virtual substrate peak and the superlattice satellites. Ge content and strain state were obtained by using the known lattice parameters for relaxed SiGe alloys [79] and interpolated elastic constants of Si and Ge [80]. The final composition of the VS was found to be 79.9% with an in-plane strain of 0.05%). The in-plane lattice parameter of the MQW stack is 0.5611 nm, the same as that of the virtual substrate, meaning that the MQW stack is coherently matched to the virtual substrate. Diffraction peaks from the VS and MQW structure are broadened perpendicular to the relaxation line due to mosaicity in the virtual substrate. The reciprocal space maps are shown in fig. 3.2. The lattice parameters and the alloy concentrations extracted from the HR-XRD measurements have been

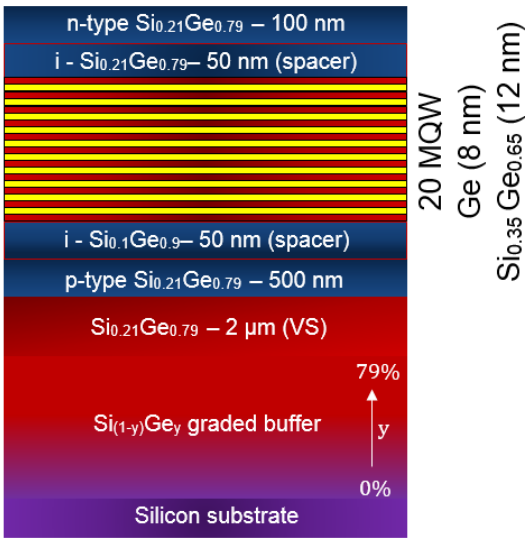

Figure 3.1: Schematic cross section of the sample with detailed growth steps.

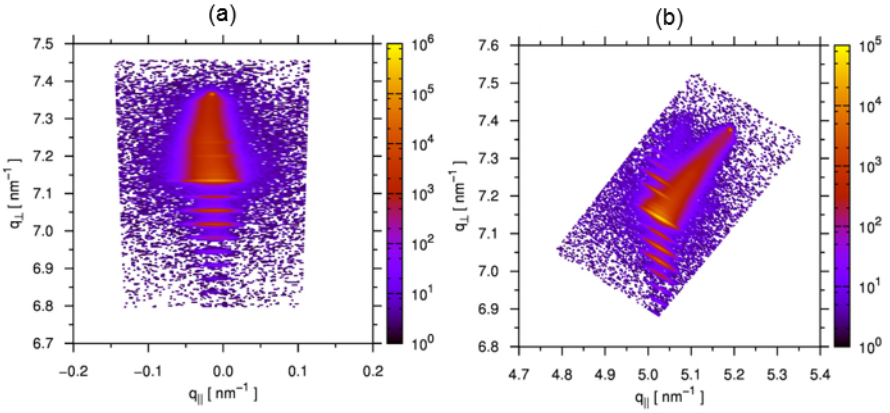

Figure 3.2: Reciprocal space maps of the sample about the 004 (a) and the 224 (b) reflections.

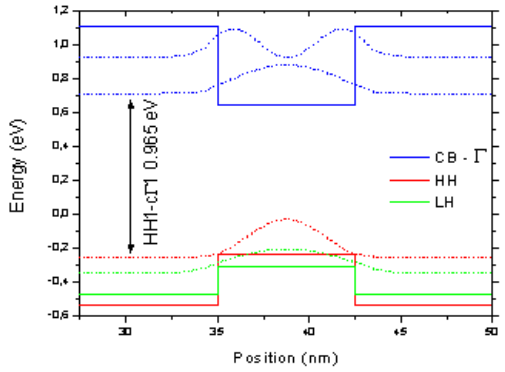

Figure 3.3: Simulated band-structure of the sample.

used to model the band structure of the sample through the NextNano software. The high in-plane compressive strain in the well (0.6 %) pushes the HH1-cΓ1 transition at 0.965 eV, which corresponds to a wavelength of 1285 nm. In Fig 3.3 the simulated band structure and squared wavefunctions are reported.

3.1.3 Photocurrent Measurements

After the growth, the sample was processed into a square p-i-n diode (100 μm x 114 μm) by UV lithography and dry etching. Metal contacts were formed evaporating 10 nm of Cr followed by 300 nm of Au. Photocurrent measurements were performed at room temperature in a surface illuminated configuration. Randomly polarized light was shined by a tunable laser perpendicular to the QW plane. The spectrum was recorded from 1.25 μm to 1.35 μm with a 1 nm resolution, and the power of the laser was 0.5 mW. A chopper and a lock-in amplifier were used to modulate the light intensity at 0.5 kHz and to collect the photocurrent. The photocurrent spectra are reported in Fig. 3.4. A clear exciton peak is visible at 1277 nm, in good agreement with the calculations. The HWHM is approximately 12 meV, slightly larger than the 7 meV obtained for $Ge/Si_{0.15}Ge_{0.85}$ MQW on $Si_{0.1}Ge_{0.9}$ VS[83]. The larger HWHM of the exciton peak observed in the considered heterostructure is due a reduction of the Γ valley

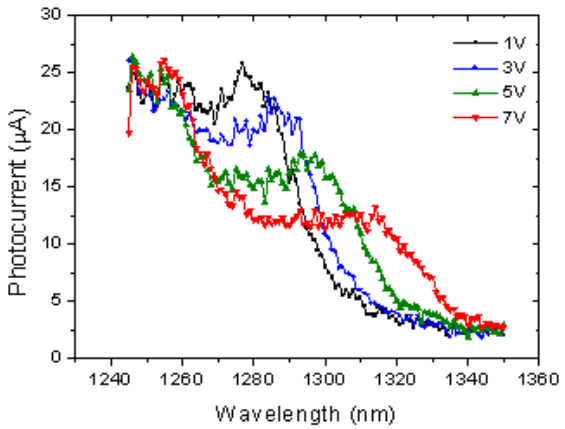

Figure 3.4: Photocurrent spectra.

lifetime resulting by the Γ-Δ intervalley scattering. This scattering channel is not active in standard strain balanced $Ge/Si_{0.15}Ge_{0.85}$ MQW, where the Γ valley lifetime is set only by the Γ-L intervalley scattering. This phenomenon will be discussed in detail in the next section. As the applied electric field is increased, the two main features of QCSE are observed. The absorption peak shifts towards longer wavelengths following with a quadratic dependendece over the electric field, and the exciton gradually broadens.

3.1.4 The role of Γ-Δ scattering

In this section, following the work of Lever et al. [84], the role of Γ-Δ scattering on the Γ valley lifetime is analyzed and discussed. The scattering lifetime is a very important parameter to be considered for QCSE based modulators, because it sets the broadening of the excitonic peaks, and consequently the extinction ratio. The first aspect to be considered is the significant splitting of the Δ valley caused by the large strain present in MQW grown on substrates with a large Si fraction. As it can be seen in Fig. 3.5, there is a remarkable splitting between the in-plane Δ_4 and the out-of-plane Δ_2 valleys with increasing Si fraction in the

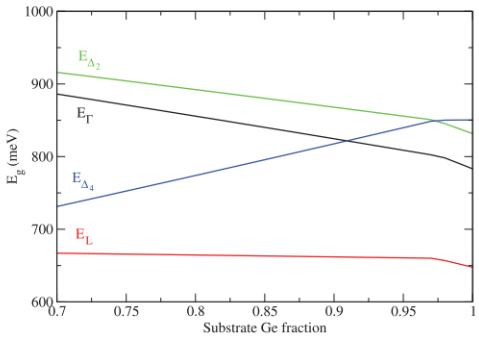

Figure 3.5: Energies of the conduction band valleys in function of the Ge fraction in the virtual substrate [84].

VS, and consequently with increasing compressive strain in the well. The Γ-Δ_4 scattering is allowed if the Ge fraction in the VS is less than 90%, thus the Γ valley lifetime in $Ge/Si_{0.4}Ge_{0.6}$ MQW grown on a $Si_{0.22}Ge_{0.78}$ VS is significantly reduced by the presence of this scattering channel. In their simulations, the authors noticed that the amount of broadening of the excitonic peak tends to increase as the well width is reduced, meaning that, as the confinement energy of the Γ electrons increases, the lifetime decreases. This happens because there is a larger density of final states in the L and Δ valleys available for electrons to scatter into. The lifetime as a function of the energy of the Γ valley subband relative to the top of the valence band is reported in fig. 3.6. Even if technological issues like threading dislocations and interface roughness appear likely to affect the excitonic peak broadening, the results of these calculations imply that the Γ-Δ scattering is an important contribution to the Γ lifetime, and the calculated lifetimes in these highly strained Ge/SiGe MQW are less than 50 fs.

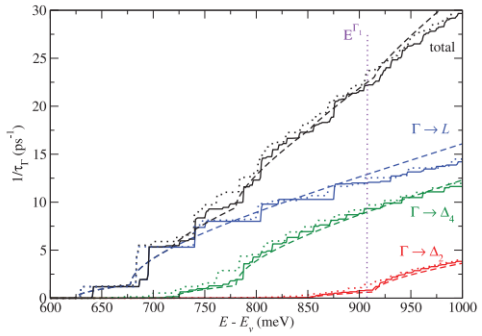

Figure 3.6: Inverse Γ valley scattering lifetime components as a fuction of the the energy of the Γ valley subband relative to the top of the valence band [84].

3.2 Electro-Refractive effect in Ge/SiGe MQW

3.2.1 Introduction

Intensity modulation is the simplest modulation format, namely on/off keying or OOK. High level modulation formats such as QPSK are strongly needed in modern telecommunication systems and they are accesible only by the manipulation of the phase of the light beam. In this section, our work on phase modulation based on QCSE in Ge/SiGe QW is presented. As discussed in the first chapter, QCSE causes strong variations in the absorption spectrum of a MQW based device. These variations must be related to a change of the refractive index, as stated by Kramers-Kronig relations:

$$\Delta n(\lambda) = \frac{\lambda^2}{2\pi^2} \int \frac{\Delta\alpha(\lambda')}{\lambda^2 - \lambda'^2}\, dx \tag{3.1}$$

Large changes in the refractive index would make Ge/SiGe MQWs attractive for the fabrication of electro-optic devices requiring phase shifters. For a given combination of Ge/SiGe MQW and SiGe virtual substrate, the electro-refractive (ER) effect is able to work at longer wavelengths with respect to those of the electro-absorption, constituting a powerful approach to extend the operative wavelengths of modulators based on this material system.

3.2.2 Sample growth and characterization

The structure was deposited on a 100 mm p-Si(001) substrate with a resistivity of 1-10 Ωcm. Before heteroepitaxy, the native silicon doxide was removed by dipping the substrate in aqueous hydrofluoric acid solution (HF:H2O 1:10) for 30 s. The first part of the structure is made by an 13 μm thick $Si_{1y}Ge_y$ graded buffer, deposited at a rate of 5-10 nm/s, in which the Ge concentration y is linearly increased from 0% to 90% with a grading rate of 7%/μm and capped with a 2 m $Si_{0.1}Ge_{0.9}$ layer forming a fully relaxed virtual substrate. The graded buffer was grown in 180 steps. In each step the germanium concentration was raised by 0.5% by increasing the GeH_4 flow while keeping costant the flow of SiH_4. As the amount of process gases increases, the deposition rate also increases. The grading rate was maintained constant by varying the time of each step according to the depostion rate. The threading dislocation density in the VS was $6\times$ 10^6 cm^{-2} as measured by chemical defect etching. A 500 nm boron doped (10^{19} cm^{-3}) $Si_{0.1}Ge_{0.9}$ layer was deposited to form the p-type contact region, followed by a 50 nm $Si_{0.1}Ge_{0.9}$ spacer. The MQW structure consists of 20 periods of 10 nm thick Ge QWs and 15 nm thick $Si_{0.15}Ge_{0.85}$ barriers grown at 475C at a rate of 1 nm/s. The individual layer thicknesses were designed in order to compensate the compressive strain in the Ge well with the tensile strain in the barrier. Finally a 50 nm $Si_{0.1}Ge_{0.9}$ layer spacer and 100 nm phosphorus doped (10^{19} cm^{-3}) $Si_{0.1}Ge_{0.9}$ layer were deposited. A cross section of the device showing detailed epitaxy steps is reported in Fig.3.7. As for the previous sample, layer compositions and strain states were measured by high-resolution X-ray diffraction (HR-XRD) reciprocal space mapping (RSM) about the (004) and (224) reflections. The final composition of the VS was found to be 92% with an in-plane strain of 0.087%). The in-plane lattice parameter of the MQW stack is 0.5634 nm, the same as that of the virtual substrate, meaning that the MQW stack is coherently matched to the virtual substrate. The reciprocal space maps are shown in fig. 3.8.

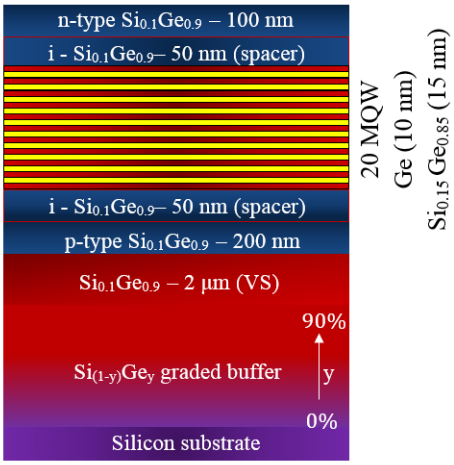

Figure 3.7: Schematic cross section of the sample with detailed growth steps.

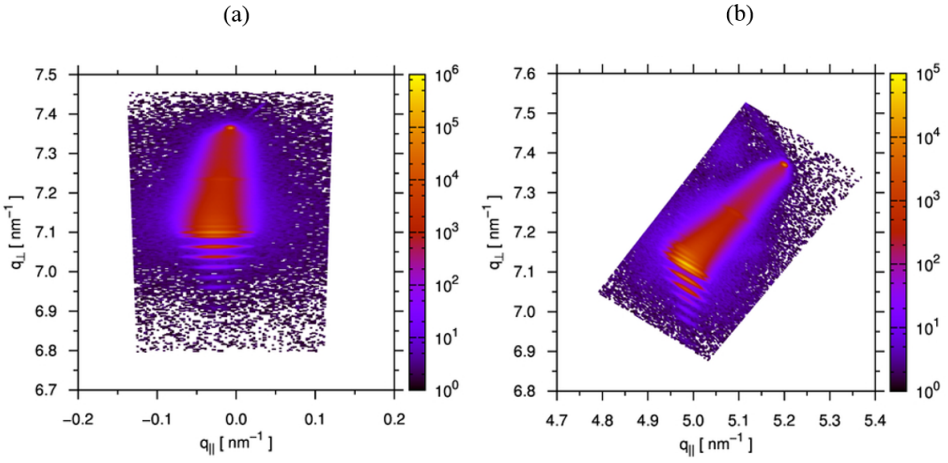

Figure 3.8: Reciprocal space maps of the sample about the 004 (a) and the 224 (b) reflections.

3.2.3 Device processing

In order to investigate the electro-refractive effect in Ge/SiGe MQW, absorption measurements were performed on 64 μm long, 100 μm wide planar waveguides. The waveguides were processed by UV lithography and dry etching. The side-wall roughness of the etched mesa was also smoothened by hydrogen peroxide (H_2O_2) solution. A few tens of nanometers of silicon dioxide were deposited by PECVD to serve as a passivation layer on the left and right walls of the waveguide. To form metal contacts, 600 nm of Al were evaporated and lifted off for both p and n layers. The top contact covers only part of the waveguide slab to minimize absorption from the metal. As the waveguide length is 64 μm, a deep etch of 90 μm was performed to bring the input fiber and output objective to the input and output facets of the waveguides. A cross section of the device is shown in Fig. 3.9.

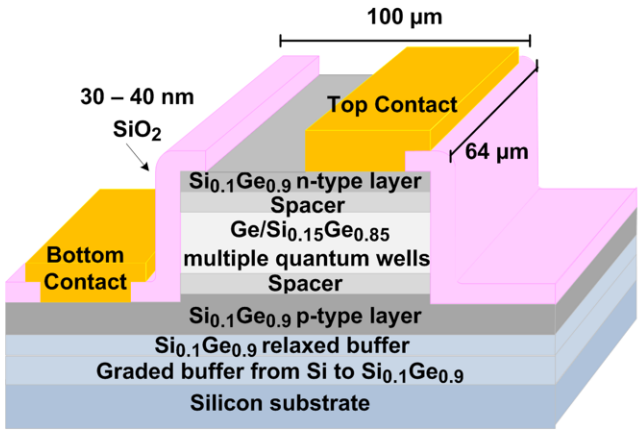

Figure 3.9: Cross section of the device used for the characterization of the electro-refractive effect. Reproduced from [85].

3.2.4 Experimental charachterization of the ER effect

The absorption measurements were performed at room temperature with a spectral resolution of 0.1 nm by using a tunable laser emitting light from 1390 to 1540 nm with a power of 1 mW. Light from the laser was butt coupled into the planar waveguide by using a taper-lensed fiber, which was placed to inject light in the waveguide region not covered by the top metal contact to reduce optical losses. An objective was used to couple the output light into a photodiode. The spectra were recorded only for TE polarized light. A scheme of the experimental set-up used is shown in Fig. 3.10 and the absorption spectra of the device in for different applied electric fields is shown in Fig. 3.11. After each measurement at a given electric field, a measurement at 0V was done to check for the absence of thermal induced shift. The current voltage characteristic of the device is reported in the inset of Fig.3.11. The absorption edge is shifted from the 0.8 eV of bulk Ge due to both the confinement effect and the compressive strain in the Ge well. Without bias voltage, an exciton peak related to the transitions between the first heavy hole subband and the first electronic level in the conduction band at the point (HH_1-$c\Gamma_1$) is observed at 0.888 eV. By increasing the applied electric field, two main characteristics of the QCSE are observed: the Stark shift of the absorption spectra and the reduction of the exciton related ab-

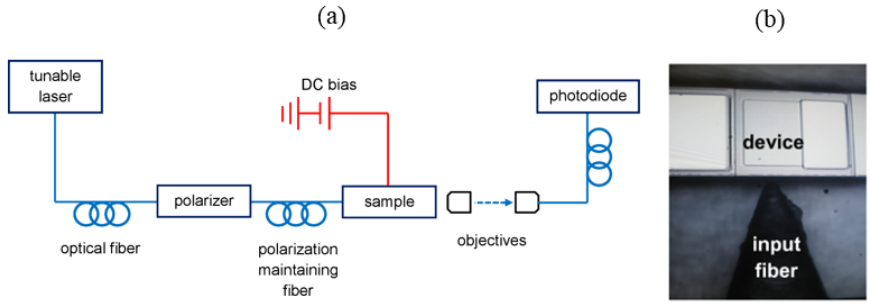

Figure 3.10: Diagram of the experimental set-up used to perform absorption measurements of the device.

sorption peak due to the reduction of the overlap between the electron and hole wavefunctions. Fabry-Perot (FP) fringes coming from the optical cavity formed between the facets of the waveguide are observed at the energy below HH_1-cΓ_1 transition.FP fringes shift when a voltage is applied to the device.In Fig. 3.12 a clear shift of the FP fringes at wavelengths comprised between 1480 nm-1490 nm can be observed for an applied voltage of 8V. The measurement of such a shift allows the determination of the refractive index change in this wavelength region. FP fringes are less pronounced around the excitonic energy because of the high optical absorption. In a cavity, the resonance condition determines the wavelength of the maxima (λ_p)in the transmission spectra according to the expression:

$$2n_{eff}(\lambda)L = p\lambda_p \tag{3.2}$$

where L is the device length, n_{eff} is the effective index of the guided mode and p is an integer number representing the order of the transmission peak. Taking

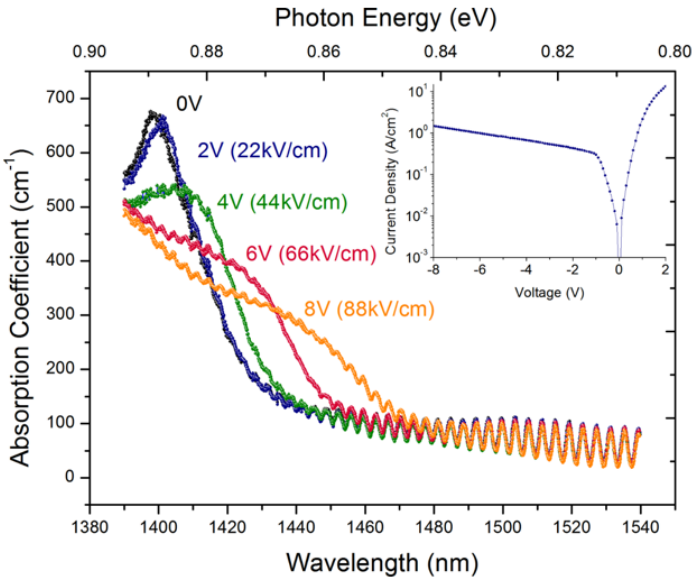

Figure 3.11: Absorption spectra of the device for different applied bias voltages. The current-voltage curve is reported in the inset. Reproduced from [85]

into account the dispersion properties of the medium, a shift $\Delta\lambda$ is related to the effective refractive index variation by:

$$\Delta(n_{eff}(\lambda) = \frac{\Delta\lambda}{\lambda} n_g(\lambda) \tag{3.3}$$

The group refractive index $n_g(\lambda)$ can be experimentally deduced from the longitudinal mode spacing $\Delta\lambda_p$ by:

$$n_g(\lambda_p) = \frac{\lambda_p^2}{2L\Delta\lambda_p} \tag{3.4}$$

The effective refractive index variation Δn_{eff} was then obtained from Eq. 3.4 by using the experimentally measured values of $\Delta(\lambda)$ and $n_g(\lambda)$, and is reported in Fig. 3.13, for different wavelengths from 1475 to 1517 nm. At each wavelength, a quadratic dependence of the effective index variation upon the electric field is observed, which is consistent with the QCSE as also observed by Wiener et al [90] and by Glick et al.[90] in MQW based on III-V semiconductors. The quadratic electro-optic coefficient s can be calculated by fitting the refractive

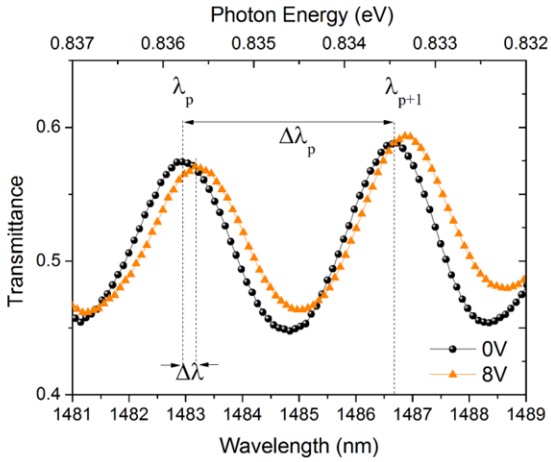

Figure 3.12: Transmission spectra at 0V (black spheres) and 8V (orange triangles) bias for wavelengths between 1480nm and 1490 nm. Reproduced from [85].

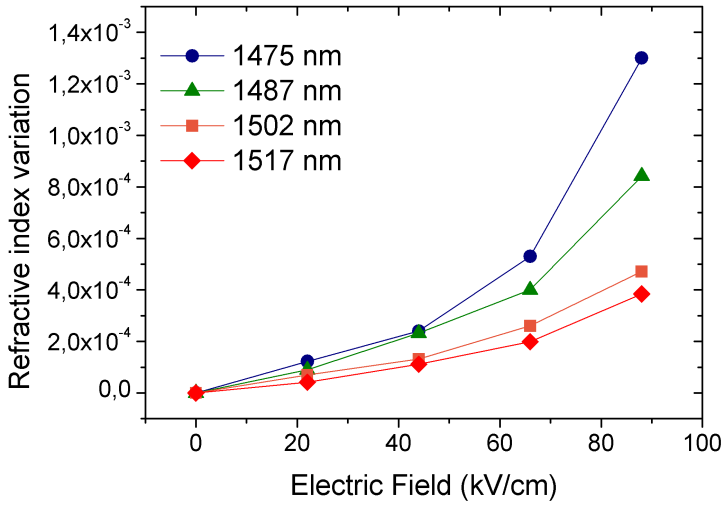

Figure 3.13: Refractive index variation as a function of the applied electric field for different wavelengths.

index variation as a function of the electric field for a given wavelength as:

$$\Delta n_{eff} = \frac{1}{2} n_0^3 \Gamma s E^2 \tag{3.5}$$

where s is the quadratic electro-optic coefficient, n_0 and Γ are respectively the average refractive index and the confinement factor of the fundamental TE mode in the MQW region. Optical mode calculations were performed to evaluate Γ, assuming that the refractive index in the graded buffer is linear from Si to $Si_{0.09}Ge_{0.91}$, and that the 10 nm Ge 15 nm $Si_{0.15}Ge_{0.85}$ MQW region is equivalent to a $Si_{0.09}Ge_{0.91}$ homogeneous region. The overlap factor of the fundamental TE mode and the MQW region was then calculated to be 17%, as it can be noticed from Fig. 3.14. The quadratic electro-optic coefficient deduced from equation 3.6 is reported in Fig. 3.15. At $\lambda = 1475$ nm a quadratic electro-optic coefficient of $(0.25 \pm 0.01) \times 10^{-18} m^2/V2$ was obtained. This value is comparable to that measured for III-V based MQW at the same spectral separation ($\sim$ 50 meV) from the excitonic resonance [90]. As the operative wavelength increases,

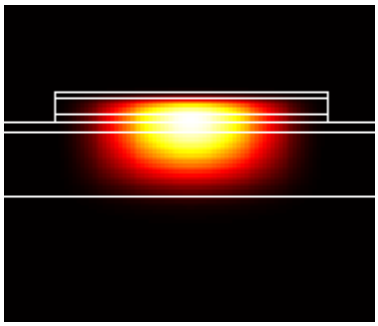

Figure 3.14: Fundamental TE optical mode distribution in the MQW structure. Since the VS and the MQW region have the same refractive index, it can be noticed that the optical mode is strongly leaking in the VS, and the overlap between it and the MQW region is only 17%.

a reduction of the effective refractive index variation and thus, of the quadratic electro-optic coefficient is observed consistently with Kramers-Kronig relations.

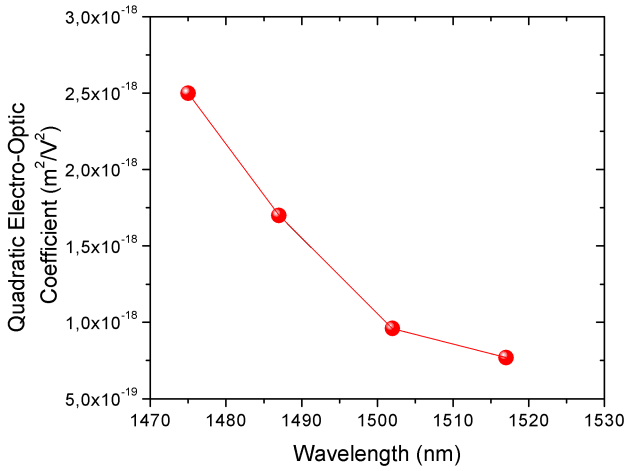

Figure 3.15: Calculated quadratic-electro optic coefficient for 10 nm Ge and 15 nm $Si_{0.15}Ge_{0.85}$ MQW.

3.2.5 Evaluation of the device performance

In order to investigate the viability of a phase-shifter based on this device architecture, the device lenght necessary to achieve a π phase shift was calculated with the following formula:

$$L_\pi = \frac{\lambda}{2\Delta n_{eff}} \tag{3.6}$$

The results are reported in Fig. 3.16. For $\lambda = 1475$ nm, the L_π is 570 μm for an applied electric field of 8.8$\times$ 10^4 V/cm with a corresponding $V_\pi L_\pi$ figure of merit of 0.46 Vcm. This value is comparable with the published values of Mach Zehnder modulators based on GaAs/AlGaAs MQW (0.55 Vcm) [86], and competitive with those of silicon (3.3 Vcm) [87]. It is worth noting that residual absorption of 50 cm^{-1} 100 cm^{-1} is observed in the spectral region above the excitonic resonance. However, as shown in ref. 88, the indirect-gap related absorption of the Ge/SiGe MQW at 50 meV from the excitonic resonance is expected to be lower than what we measured in this work. For this reason, the residual absorption has been mainly attributed to the indirect interband transitions in the Ge-rich part of the VS, and may be reduced by increasing of the overlap factor of the guided mode with the MQW region.

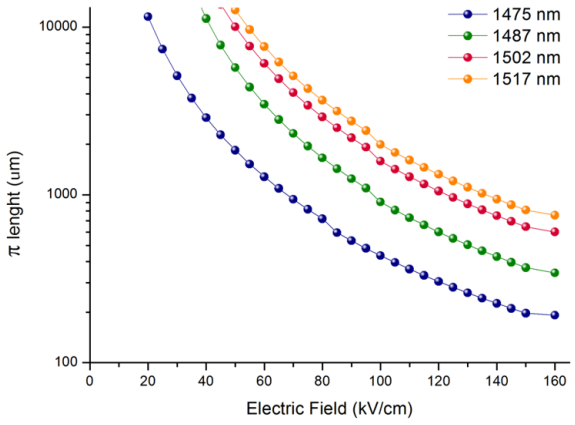

Figure 3.16: Calculated L_π for the device. This parameter represent the device lenght necessary to achieve a π phase shift for a given applied voltage.

3.3 Ge/SiGe MQW photonic interconnection

3.3.1 Introduction

One of the main problem to be addressed regarding Ge/SiGe MQW based modulators is their integration with other passive optical components such as waveguides. As mentioned in the third chapter, many efforts have been made in order to find an efficient way to couple the MQW structure with silicon waveguides. In this section, a different approach based on the use of the virtual substrate as a low-loss waveguide is presented. By choosing a suitable compositional mismatch between the MQW stack and VS, it is possible to minimize the optical losses in the waveguide at the modulation wavelength. A photonic interconnection made by a Ge/SiGe MQW modulator connected to a Ge/SiGe MQW photodetector through a SiGe waveguide has been fabricated and tested in order to demonstrate the great potential of this new approach.

3.3.2 Sample growth and charachterization

The deposition has been performed by LEPECVD on a 4-inch p-type silicon wafer. The first part of the structure is made by an 11 m thick $Si_{1y}Ge_y$ graded buffer, deposited at a rate of 5-10 nm/s, in which the Ge concentration y is linearly increased from 0% to 83% with a grading rate of 7%/μm. The VS is made by an 1.5μm thick $Si_{0.16}Ge_{0.84}$ layer. The slight compositional mismatch with respect to the top of the graded buffer has been designed in order to obtain a better confinement of the optical mode in the VS. A 200 nm boron doped (10^{19} cm^{-3}) $Si_{0.09}Ge_{0.91}$ layer was deposited to form the p-type contact region, followed by a 50 nm $Si_{0.1}Ge_{0.9}$ spacer. The MQW structure consists of 10 periods of 12 nm thick Ge QWs and 16 nm thick $Si_{0.16}Ge_{0.84}$ barriers grown at 450C at a rate of 1 nm/s. Finally a 50 nm $Si_{0.1}Ge_{0.9}$ layer spacer and 100 nm phosphorus doped (10^{19} cm^{-3}) $Si_{0.1}Ge_{0.9}$ layer were deposited. A cross section of the device with detailed epitaxy steps is reported in fig. 3.17. The Ge content in the VS has been chosen in order to minimize the optical absorption at 1450

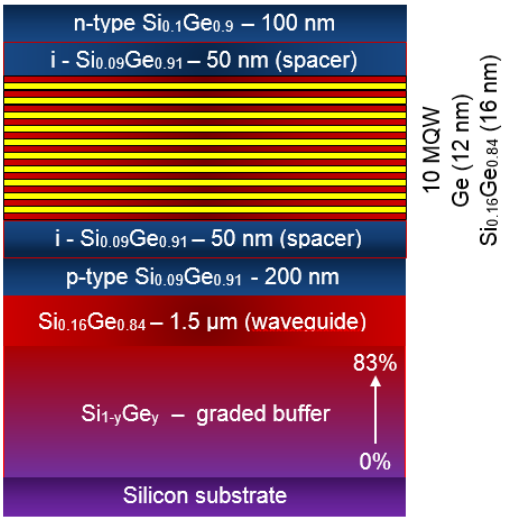

Figure 3.17: Cross section of the sample used to realize the optical interconnection.

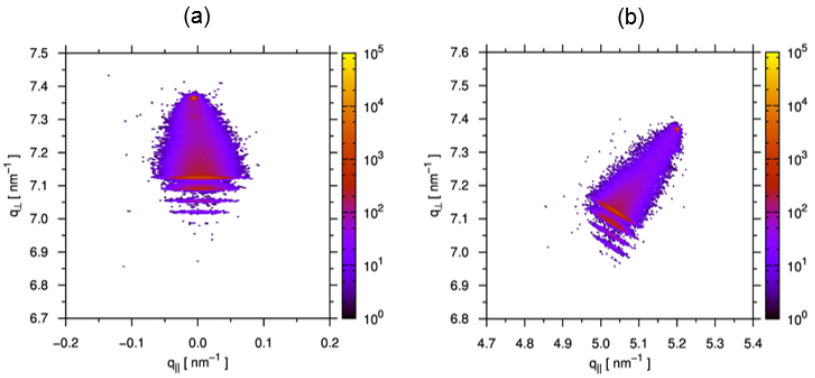

Figure 3.18: Reciprocal space maps of the sample about the 004 (a) and the 224 (b) reflections.

nm[91], which is the working wavelength of the MQW modulator according to the simulations. At the same time, the compositional mismatch between the VS and the MQW stack is low enough to avoid the introduction of new misfit dislocations at the interface. The structural properties of the sample have been determined by HR-XRD (See fig. 3.18). The VS and the 0^{th} order superlattice peak do not share the same $q_{||}$ because of the compositional mismatch. Nevertheless, the sharp satellite peaks indicate a good crystal quality for the MQW stack.

3.3.3 Device processing and Measurements

Three differnt devices have been fabricated: (i) $Si_{0.16}Ge_{0.84}$ waveguides with different lenghts; (ii) a $Ge/Si_{0.16}Ge_{0.84}$ MQW p-i-n diode and (iii) a photonic interconnetion made by a $Ge/Si_{0.16}Ge_{0.84}$ MQW modulator and photodetector connected by a $Si_{0.16}Ge_{0.84}$ waveguide. All the devices have been patterned by UV lithography and dry etching. The photodiode and the modulator were also passivated with Si_3N_4 and SiO_2 deposited by PECVD and metallized to create electrical contacts.

$Si_{0.16}Ge_{0.84}$ waveguides

The waveguides have been fabricated and tested in order to determine the optical losses. Rib waveguides 2 μm wide and 1.5 μm thick were processed with lenghts of 750, 1250, 1750, 2250, and 2750 μm (see fig. 3.19). As shown in fig. 3.20, optical losses of 5dB/cm and of 2dB/cm can be obtained at wavelengths longer than 1410 and 1440 nm respectively. In order to determine the losses of the waveguides, optical transmission measurements have been performed on each waveguide in the spectral range from 1340 to 1540 nm.

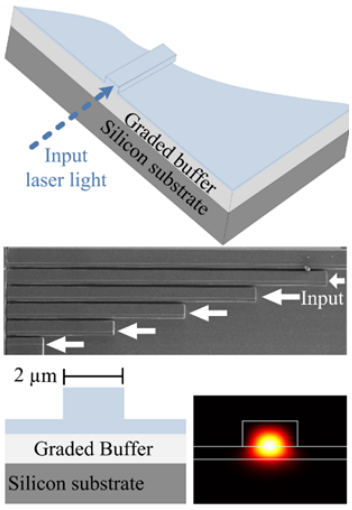

Figure 3.19: Schematic and SEM view of the waveguides.

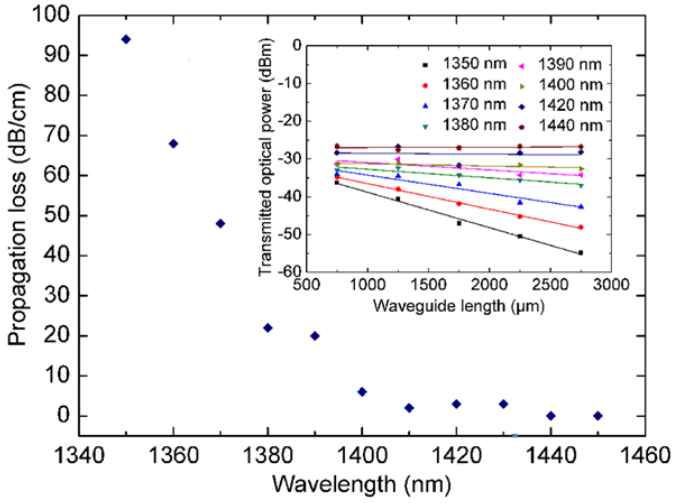

Figure 3.20: Plot of the optical losses of the waveguide. In the inset the plot of the transmitted optical power as a function of the waveguide length for different wavelengths is reported.

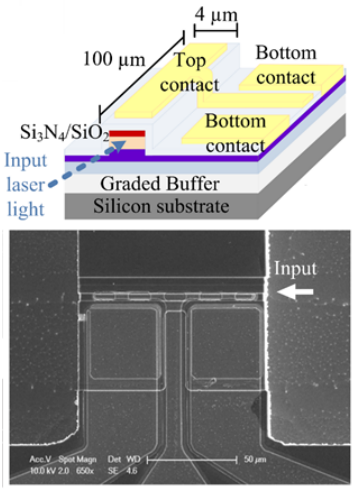

Figure 3.21: Schematc and SEM view of the stand alone MQW p-i-n diode.

Ge/$Si_{0.16}Ge_{0.84}$ MQW p-i-n diode

The stand alone p-i-n diode (see fig. 3.21) has been fabricated in order to determine the absorption properties of the Ge/$Si_{0.16}Ge_{0.84}$ MQW through photocurrent spectroscopy (see fig 3.22). A clear excitonic peak around 0.888 eV can be observed at room temperature at 0V bias. As the voltage is increased, the two main features of QCSE can be observed. The exciton related absorption peak is reduced and shifted toward longer wavelengths. A strong absorption variation can be observed at wavelengths longer than 1420 nm, where the absorption of the waveguide is low enough to allow mode propagation. The MQW used as a photodiode showed an optical responsivity up to 0.6 A/W and, as a modulator, an extinction ratio of 3.5-4 dB with insertion loss of 2-3 dB in the spectral range comprised between 1430-1450 nm. An important point to be addressed, is that the responsivity and modulation performance of the device show no degradation with respect to our previus works using strain balanced MQW. Regarding the time response of the device, cut off-frequences of 4GHz and 6.3 GHz have been obtained for photodetection and modulation respectively, as shown in fig. 3.23.

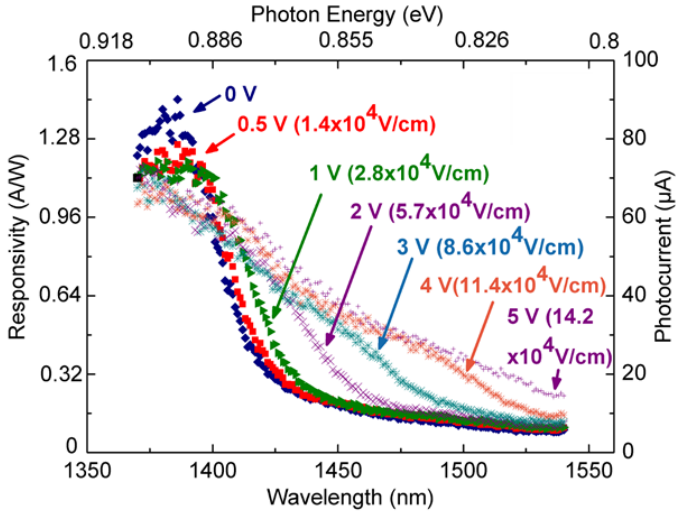

Figure 3.22: Absorption spectra of the stand alone MQW p-i-n diode with different applied voltages.

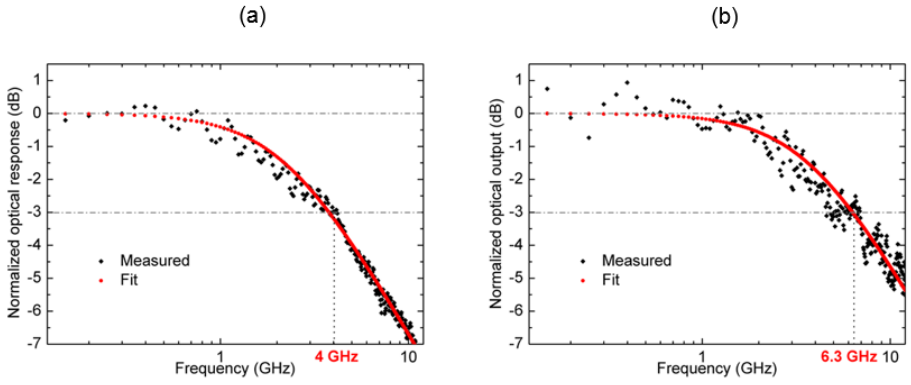

Figure 3.23: Time response of the MQW device for detection (a) and modulation (b).

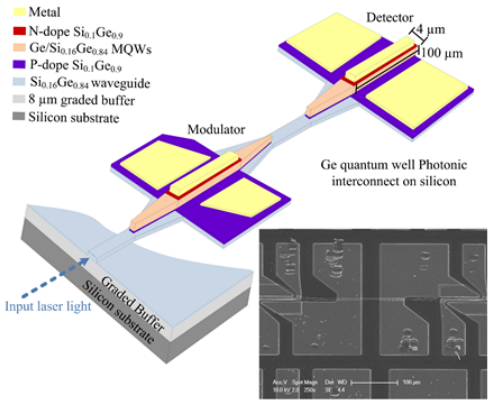

Figure 3.24: Scheme and SEM view of the processed photonic link

Photonic Interconnection

The scheme of the photonic inteconnection is reported in fig. 3.24. The IV characteristics of both the modulator and the detector are reported in Fig. 3.25(a) when the same bias voltage is applied to the devices. The measurements have been performed by using a tunable laser with an output power of 3 mW at a wavelength of 1440 nm. The photocurrent in the photodetector is lower only by a factor 3 with respect to that of the modulator, and both devices have the same size. The optical insertion loss is less than 5 dB, thus the performances of the photonic interconnect are even better than that reported for III-V devices bonded on silicon [92]. In Fig. 3.25(b) are reported the IV characterstic of the photodetector for different bias voltages applied to the modulator at 1440 nm. 5 and 10 μA between the "0" and the "1" logic levels have been obtained by using 1V and 3V voltage swing at the modulator, respectively. The photodector, biased at -1V have shown a dark current of 10 nA, thus the shot noise is only 2.5 pA/Hz$^{-1/2}$. The photonic interconnect thus has a very promising potential for low bit error rate data transmission.

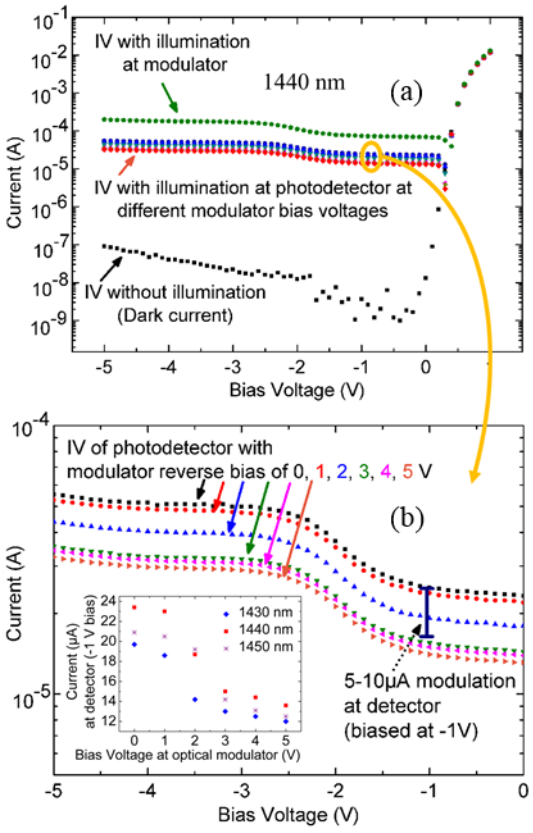

Figure 3.25: IV characteristics of the fabricated photonic interconnect (a) and photocurrents at the photodetector with different reverse bias voltages at the optical modulator.

Chapter 4

Hyghly strained Ge micro-bridges

4.1 Introduction

Tensile strain is an extremely powerful tool to engineer the Ge bandstructure in order to turn this element into an efficient light emitter. As mentioned previously, also n-type doping can be employed in order to achieve such a target, but it is associated with several drawback such as the enhancement of non radiative recombination and free carrier absorption. For this reason the research toward an efficient Ge laser is now focused on the enhancement of tensile strain through post growth approaches. In this chapter our work carried out with the team of Dr. Hans Sigg of the PSI and of Prof. Jerome Faist and Ralph Spolenak of th ETH, is presented. Our approach is based on a top-down fabrication method developed to realize highly uniaxially strained Ge microbridges on Si and on SOI. In this first work, an undoped sample was used in order to investigate the effect of an high level of tensile strain on the band structure of germanium.

4.2 Strain Enhancement

The fabrication method consists in the realization of suspended Ge microbridges (see fig. 4.1) starting from a biaxially tensile strained Ge epilayer grown on Si or on SOI. The force in the epilayer and its thickness are constant, and the stress is inversely proportional to the cross sectional area, thus the stress increases at the constricted region. After the processing, the strain state of the microbridge is uniaxial, and it depends only on the geometrical dimensions of the structure and on the growth related pre-strain, and it can be expressed as:

$$\varepsilon = \varepsilon_{bi}\eta\frac{2L+B}{B}\left[1+\frac{A}{B-A}\right]/\left[\frac{a}{b}+\frac{A}{B-A}\right] \tag{4.1}$$

wher ε_{bi} is the biaxial pre-strain, A and a are respectively the length and the width of the constriction,B and b are respectively the length and the width of the pads, L is the length of the etched region under the Ge/Si layer and η is an adimensional parameter taking into account the difference in stiffness between the Ge/Si and the Ge/SOI structures. Interestingly, as stated by the equation 4.1, the strain depends only on the ratios between the widths and lengths of the bridge and of the pads, so it is independent on the size scale. The strain enhancement is limited only by the mechanical strenght of the material.

4.3 Sample growth and characterization

The samples grown for this project are all made by a 1.5 um thick nominally undoped germanium epilayer deposited on silicon or on SOI. In this section the optimization of the growth parameters in order to obtain the maximum thermal strain is described.

4.3.1 Thermal strain

The strain state in the micro-bridge, as stated by equation 4.1, depends not only on the geometrical dimensions of the bridge but also on the thermal induced pre-strain present in the epilayer after the growth. From the technological

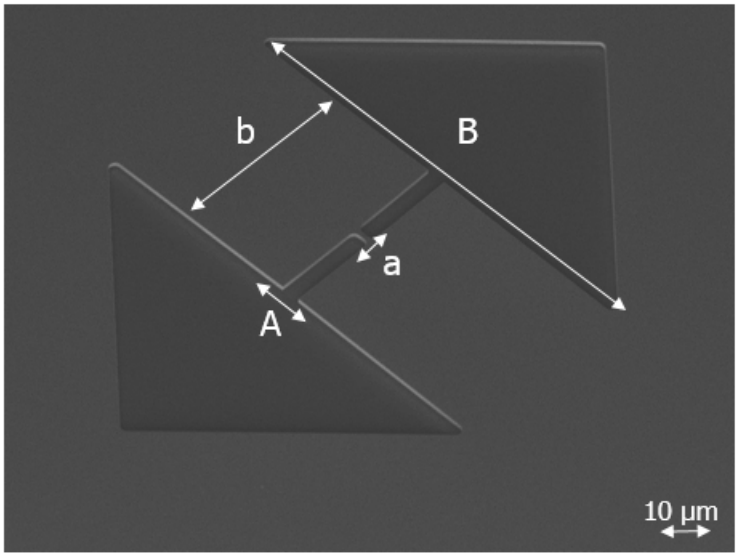

Figure 4.1: SEM view of a microbridge. In the figure the main geometrical parameters are indicated.

point of view, the maximimum thermal strain achievable depends on the maximum temperature reached during the annealing procedure and on the cool-down rapidity. A series of four samples were grown in order to optimize the annealing procedure. All the samples have been grown by LEPECVD on 4-inch Si substrates. They consist in a 1.5μm thick nominally undoped germanium epilayer grown at 500^o at intermediate rate. The maximum substrate temperature achievable in the LEPECVD reactor is around 800^{o}C. For this reason, in order to maximize the thermal strain, we have used an external rapid thermal annealing tool to perform the annealing procedure. The five samples were annealed at different temperatures in a forming gas atmosphere. After the annealing, the strain state was charachterized by HR-XRD (see fig. 4.2) and the surface roughness was measured by atomic force microscopy (see fig. 4.3). A trade-off between the surface quality and the thermal strain is expected, thus the aim of this experiment was to find the optimal annealing temperature. The results are summarized in tab 4.1. From the XRD analysis, it can be noticed the the

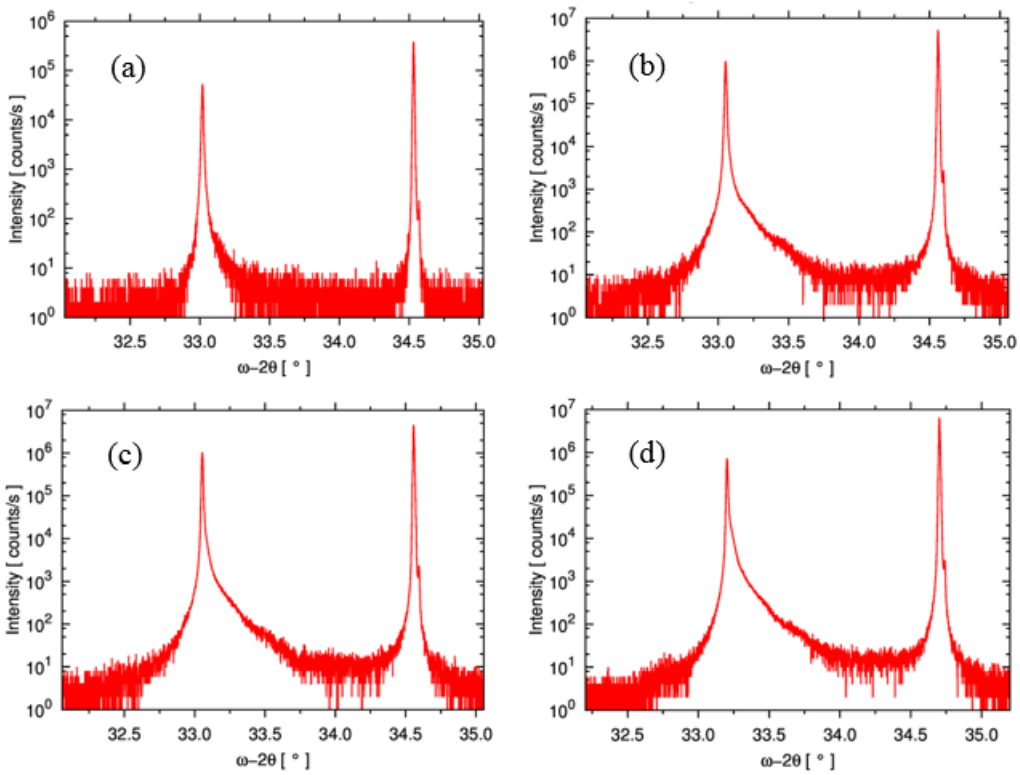

Figure 4.2: HR-XRD ω-2θ scans of the four samples used for the optimization of the annealing procedure. The annealing temperatures are (a) 750^{o}C, (b) 800^{o}C, (c) 850^{o}C, (d) 900^{o}C.

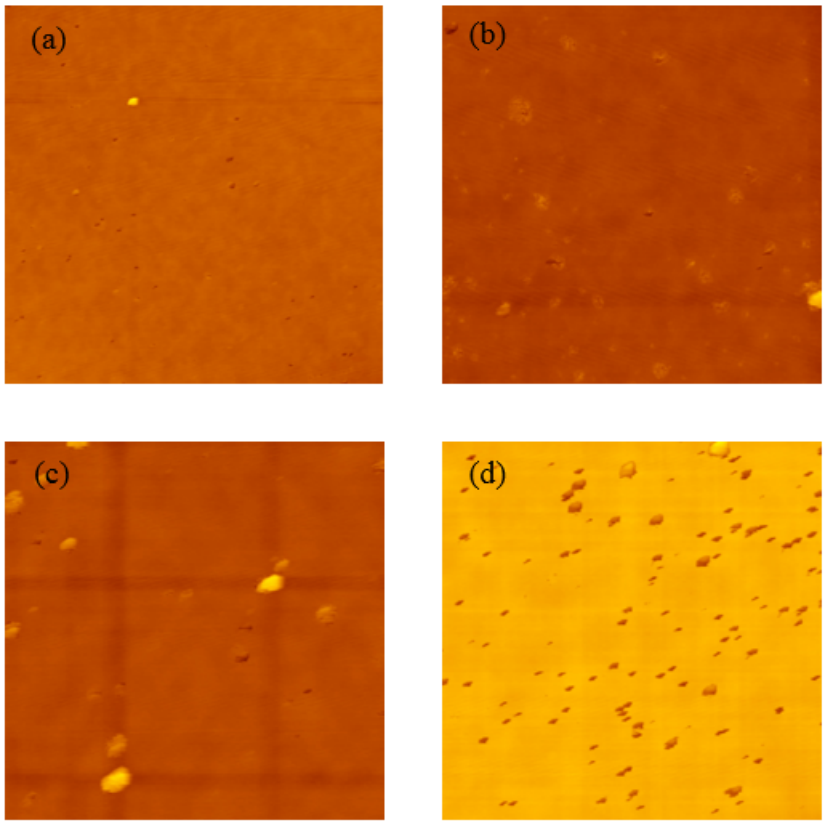

Figure 4.3: AFM scans of the four samples used for the optimization of the annealing procedure. The annealing temperatures are (a) 750^{o}C, (b) 800^{o}C, (c) 850^{o}C, (d) 900^{o}C. The area of the AFM scans is 30μm $\times$ 30μm.

Sample	Annealing Temperature (^{o}C)	Tensile Strain (%)	surface roughness (nm)
A	750	0.19	0.92
B	800	0.21	1.56
C	850	0.22	2.15
D	900	0.22	2.52

Table 4.1: Results of the annealing procedure optimization

thermal tensile strain present in the epilayer saturates at 0.22%, reached for an annealing temperature of 850 ^{o}C. Moreover, the AFM scans show the presence of holes on the surface for the sample D, annealed at 900^{o}C. Thus the optimal annealing temperature was found to be 850^{o}C.

4.4 Fabrication of the micro-bridge

The sample used for this work was grown by LEPECVD on an SOI substrate. The substrate have a 1μm thick SiO_2 BOX layer and a 340 nm thick Si device layer. The sample consists in an 1.5 μm thick nominally undoped germanium layer grown at approximately 1 nm/s at a temperature of 500^{o}C. After the growth, thermal annealing cycles were performed in order to reduce the threading dislocation density. A schematic cross section of the sample is shown in fig. 4.5. The sample was then characterized by HR-XRD. The biaxial strain was 0.18 %, which is slightly lower with respect to what obtained with silicon substrates because of the different stiffness of the SOI. The reciprocal space maps are shown in fig 4.6. After the growth, the sample was covered by 60 nm of Cr. The micro-bridge structures were then patterned using PMMA and standard electron beam lithography. After dry etching of the Cr mask, the Ge and Si layers were etched down to the BOX with SF_6-based reactive ion etching. The final structures were released from the substrate by hydrofluoric acid. A scheme of the main fabrication steps is shown in Fig. 4.7.

Figure 4.4: Schematic view of the sample with detailed epitaxial steps.

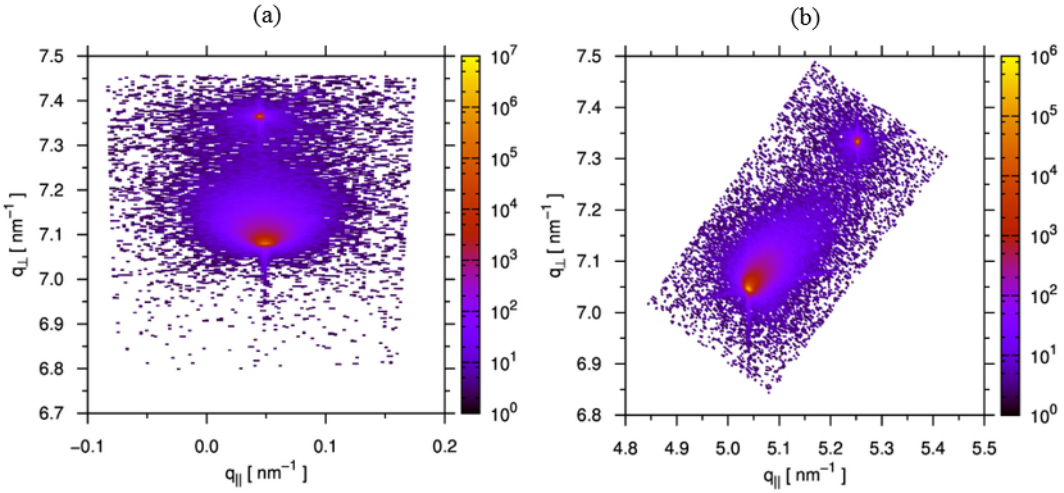

Figure 4.5: Reciprocal space maps of the sample about the 004 (a) and 224 (b) reflections.

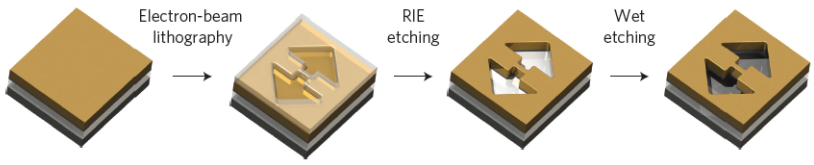

Figure 4.6: Schematic view of the main steps of the micro-bridge fabrication process [91].

4.5 Raman measurements

The strain state of the micro-bridge was measured by Raman spectroscopy. The spectra were recorded in different positions on the suspended Ge/SOI structure, and the results are plotted in fig 4.8. The spectrum for bulk unstrained germanium (black dashed curve) is plotted as a reference. The peak measured far from the bridge structure (red peak) is shifted by 0.65 cm^{-1} with respect to the bulk, corresponding to a biaxial strain of 0.18%. The peak related to the constriction (green curve) is shifted by about -4.8% with respect to the bulk reference. This value corresponds to a longitudinal strain ε_{xx} of 3.1%. Interestingly, the peak measured on the pad (blue curve) is very close to the unstrained bulk reference, meaning that the strain in the constriction is accumulated at the expense of relaxation in the pads.

4.6 Photoluminescence measurements

In Fig. 4.9 are reported the micro-photoluminescence spectra recorded at room temperature in different micro-bridge structures with different strain levels. The excitation power was 4.5 mW from a laser source operating in continuous wave at a wavelength of 532 nm. The laser spot size was set to a diameter of 0.8 μm. The oscillations in the spectra are attributed to Fabry-Perot resonances of the suspended structures, as demonstrated by the reflection spectrum shown at the bottom of fig. 4.9. Unfortunately, the identification of the contribution from several possible radiative transitions from L and Γ conduction band minima to

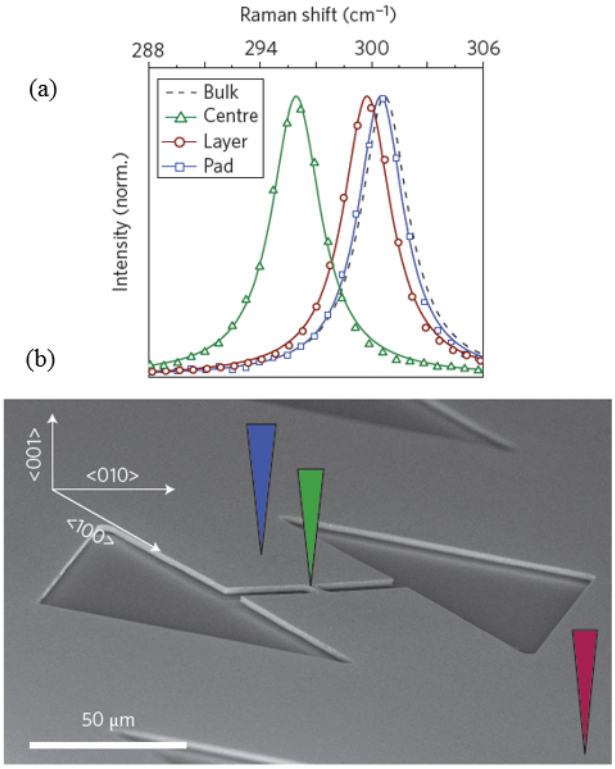

Figure 4.7: Normalized Raman spectra (a) taken at position indicated by coloured triangles in (b). Reproduced from[91].

the valence band are difficult to identify due to the presence of Fabry-Perot resonances. Nevertheless, a red-shift and an increase of the intensity of the photoluminescence peak with increasing longitudinal strain is clearly visible. For the maximum longitudinal strain (3.1%) the photoluminescence peak is shifted of 210 meV and its intensity is increased by a factor 25 with respect to the bulk reference. This is a clear indication of reduced bandgap energy as well as a decreased energy separation between the L and Γ minima.

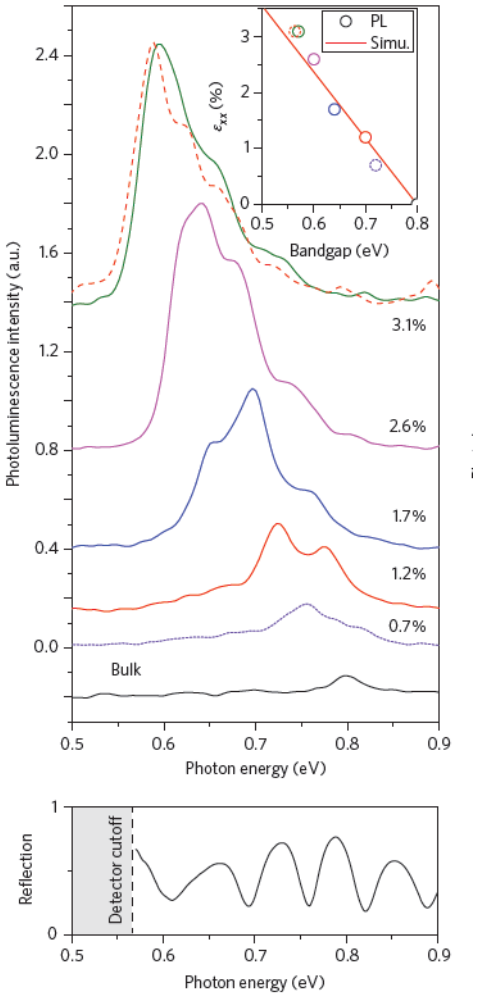

Figure 4.8: Micro-photoluminescence spectra taken from structures with increasing strain. The reflection spectrum showing Fabry-Perot resonances is reported at the bottom. Reproduced from[91].

4.7 Gain calculation

To calculate the optical gain in the micro-bridge structures, we combined the model for calculating the band structure with optical gain calculation using Fermi-Dirac statistics and Fermi's golden rule. The absorption cross sections

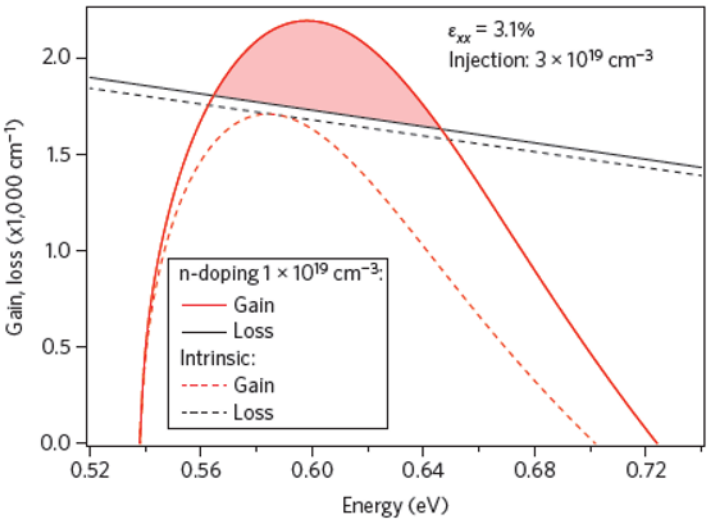

Figure 4.9: Gain simulation for 3.1% strained Ge structures doped and undoped. Reproduced from[91].

of the intraband absorption in the valence band, the main loss channel, were extracted from [64]. In fig. 4.10 is reported the energy-dependent absorption of an undoped and an n-doped (10^{19} cm^{-3} Ge epilayer with 3.1% uniaxial strain at an injection density of 3×10^{19} cm^{-3}. We find that the material gain exceeds the loss for the doped sample, but for an undoped sample as the investigated one, only the transparency can be reached.

Chapter 5

Carrier lifetime study in Ge-on-Si epilayers

5.1 Introduction

In the route toward the realization of an efficient Ge-on-Si laser, several material parameters, such as carrier induced optical loss, carrier lifetimes and non radiative recombination have to be taken into account. The properties of doped Ge-on-Si epilayers can deviate substantially from the properties known for intrinsic bulk Ge, due to the defective layer formed at the Ge/Si interface and to the doping. In this chapter, a study on excess carrier lifetime in Ge-on-Si epilayers is presented. Pump-probe transmission spectroscopy was used to extract the excess carrier lifetime on differently prepared Ge-on-Si samples. The experiment was designed in order to highlight the impact of the growth parameters, such as doping and post growth annealing, on the lifetime. The transmission measurements were performed at the X01DC beamline of the Swiss light source using the broadband synchrotron radiation as the probe pulse. Pump pulses of 100 ps were delivered by a Nd:YAG laser at a wavelength of 1064 nm. Due to multiple interferences within the layered stack, the transmission spectra are

modulated by Fabry-Perot oscillations. The photoexcited carriers change the refractive index of the material, leading to a phase shift of the oscillations. By follwing the temporal dependence of this phase shift for increasing pump-probe delay time, it is possible to extract the carrier lifetime.

5.2 N-type doping calibration

In order to highlight the impact of n-type doping on the carrier lifetime, a calibration of the n-doping was performed. The doping is obtained in-situ, by adding PH_3 to the process gas mixture during the growth. The concentration and uniformity of dopants into the epilayer depends on many growth parameters, such as the ratio between the flows of PH_3 and GeH_4, the growth temperature, the intensity of the plasma and the annealing procedure. In this section the calibration and optimization of n-type doping is presented, as well as the role of the aforementioned growth parameters.

5.2.1 PH_3/GeH_4 ratio

In order to determine the relation between the active donor concentration and the ratio between the flows of PH_3 and GeH_4, seven samples have been grown. All the samples consist in 1 μm thick Ge epilayer grown at 500^{o}C at intermediate rate on intrinsic SOI substrates. The GeH_4 flow has been kept to 20 sccm for all the samples, while the PH_3 flow has been varied for every sample. Since the growth rate is dependent on the amount of PH_3 in the gas mixture, the thickness of each sample has been measured by SEM. After the growth, the samples have been processed by UV lithography and dry etching in order to obtain six-terminals Hall bars. Finally Ti/Au contacts have been deposited by e-beam evaporation. The dopant concentration was determined for each sample by four point probe measurements. The results are summarized in tab 5.2. The dopant concentration in function of the PH_3/GeH_4 ratio is reported in Fig. 5.1. It can be noticed that the maximum dopant density is obtained for a ratio of 30%

PH_3/GeH_4(%)	Dopant concentration (cm^{-3})
0.5	1.3×10^{17}
5	3.1×10^{18}
12.5	1.0×10^{19}
20	1.9×10^{19}
25	2.1×10^{19}
30	2.3×10^{19}
35	1.8×10^{19}

Table 5.1: dopant concentration in function of the ratio of PH_3 and GeH_4

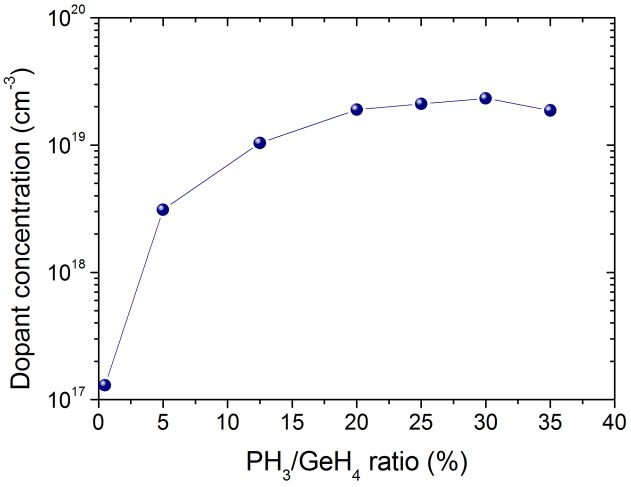

Figure 5.1: Dopant concentration (log scale) in function of the PH_3/GeH_4 ratio.

between the phosphine and germane fluxes. At higher ratios, the incorporation of dopants decreases. This has been attributed to clustering of P atoms.

5.2.2 Growth temperature

In order to investigate the influence of the growth temperature on the incorporation of dopants in the Ge epilayers, three samples have been grown by LEPECVD on intrinsic SOI substrates. The samples consist in 1μm thick Ge

Growth temperature (^{o}C)	Dopant concentration (cm^{-3})
400	2.1×10^{18}
500	2.3×10^{19}
600	2.2×10^{19}

Table 5.2: Dopant concentration in function of the growth temperature. The The GeH_4 flux was 20 sccm and the PH_3 flux was 6 sccm.

epilayers grown at intermediate rate. The GeH_4 flux was 20 sccm and the PH_3 flux was 6 sccm. The growth temperatures were 400^{o}C, 500^{o}C and 600^{o}C. Also in this case the samples were processed by UV lithography and dry etching into six-terminals Hall bars and then the dopant concentration was determined by four point probe. The results are summarized in table 5.2.

5.3 Influence of doping on the lifetime

The first experiment was designed in order to highlight the influence of heavy n-type doping on the carrier lifetime. Two samples were grown by LEPECVD on an SOI substrate. The first sample, named "iGe" consists in a 1.7 μm thick nominally undoped germanium epilayer grown at intermediate rate at a temperature of 500^{o}C. After the growth, thermal annealing cycles were perfomed in order to reduce the threading dislocation density. The second sample, named "nGe" consists in a 1.7 μm thick n-doped Ge epilayer grown at intermediate rate at a temperature of 500^{o}C. The donor concentration in this sample was 1×10^{19} cm^{-3}. Also for this sample, thermal annealing cycles were performed to improve the quality of the epilayer. In fig. 5.2 a schematic view of the samples is reported. As it can be seen from fig. 5.3, the decay time for the iGe is 2 ns while for the nGe is 0.4 ns. For the n-doped sample, a single exponential decay is obtained. Since this decay keeps its fast character also for longer times, where the carrier density is too low for three-particle process to play a significant role, this decay cannot be attributed to Auger recombination.

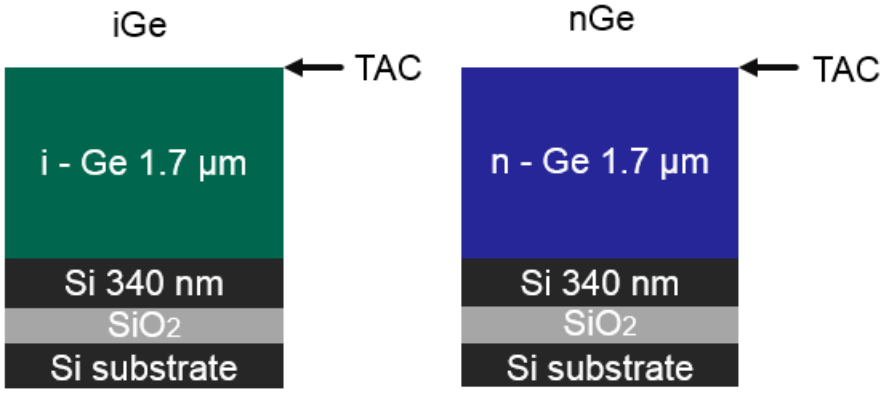

Figure 5.2: Schematic view of the iGe and nGe samples.

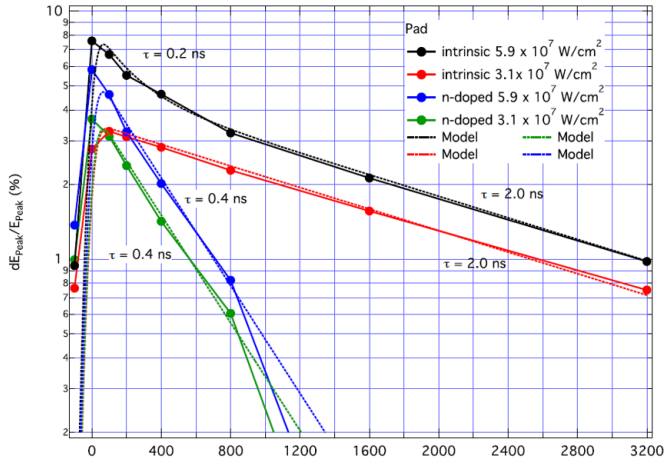

Figure 5.3: Measured decay times for iGe and nGe samples.

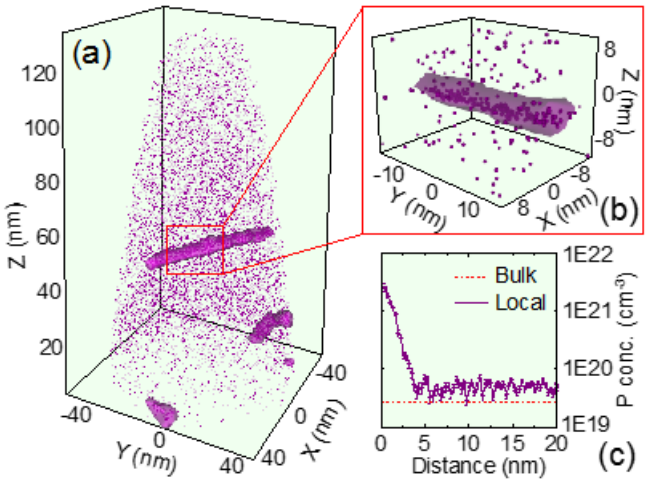

Figure 5.4: Atom Probe tomography of the nGe sample.(a) Full reconstruction displaying only the P atoms.(b) Close-up of one enriched region, likely along a dislocation line. (c) Proximity histogram from the center of the enrichment line towards the outside.

We hypothesized that the presence of an high density of P atoms in this sample is able to reduce the efficiency of the thermal annealing cycles in the reduction of threading dislocation density, but transmission electron microscopy (TEM) measurements revealed that the two samples, iGe and nGe, have exactly the same density of threading dislocations (3×10^7 cm^{-2}). Further investigations of the dopant distribution, performed by atom probe tomography, reavealed a spatial inhomogeneity of dopant distribution (see fig. 5.4). Several P clusters, preferentially formed along threading dislocations, were found by Atom Probe. Therefore, the rapid decay of the nGe sample was ascribed to the formation of impurity complexes during the annealing procedure.

5.4 Influence of the Ge/Si interface on the lifetime

After the results of the previous experiment, in order to obtain a Ge epilayer with high n-type doping and a long decay time, another sample, named "iGe/nGe" was grown. The sample, grown by LEPECVD on an SOI substrate, was made in two steps (see fig. 5.5). In the first one, a nominally undoped, 1.2 μm thick Ge layer was grown at intermediate rate at a temperature of 500^{o}C. Thermal annealing cycles were performed after the growth of this first layer in order to reduce the density of threading dislocations. The second step was to grow another Ge layer, n-doped (1×10^{19} cm^{-3}) at intermediate rate at a temperature of 500^{o}C. No annealing was perfomed after this step. In this way the formation of the impurity clusters observed for the nGe sample should be avoided. For this sample, the measured decay time was 2.6 ns, even higher with respect to that of the iGe sample. This result highlight the major role played by the defective Ge/Si interface in the determination of the carrier lifetime. Indeed, the selective doping, the sample iGe/nGe features a built-in electric field which helps to keep the photoexcited carriers in the doped region, away frome the Ge/Si interface. In order to confirm the dominance of the interface in the determination of the carrier lifetime, we have grown another sample, named "GOI". This sample was grown by LEPECVD on a germanium-on-insulator (GOI) substrate. The use of GOI substrate avoid the introduction of dislocation, since the growth is homoepitaxial. The sample consists in a 2.6μm thick nominally undoped Ge layer grown at intermediate rate at a temperature of 500^{o}C. Thermal annealing cycles were not performed for this samples. The measured decay time for the GOI sample was 5.3 ns, the highest among the considered sample. This result confirm the hypotesis that the defective Ge/Si interface is the primary reason for the reduction of the carrier lifetime. The results are summarized in fig. 5.6.

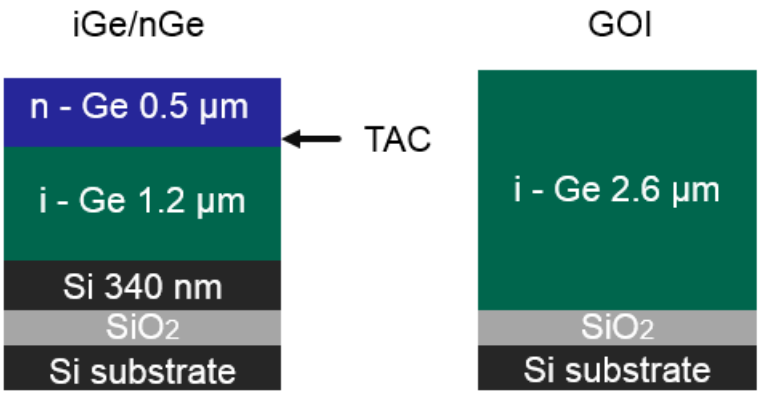

Figure 5.5: Schematic view of the iGe/nGe and GOI samples.

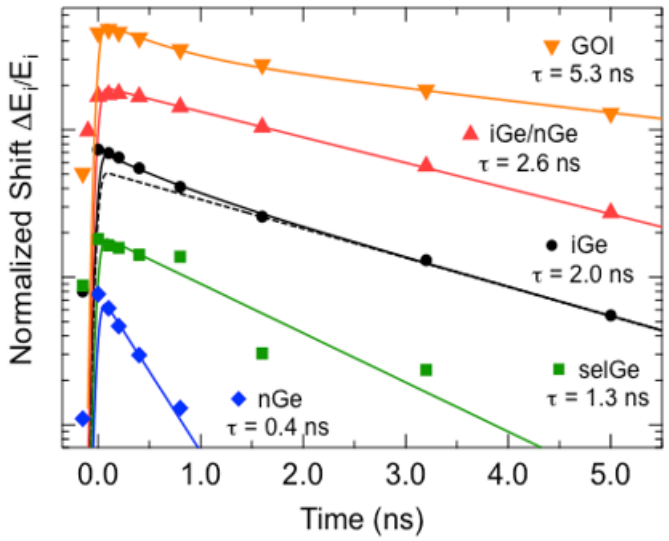

Figure 5.6: Measured decay times for all the investigated samples. The selGe sample was not included in the discussion presented here.

Conclusions

The first part of this thesis was devoted to the realization of silicon compatible modulators based on Ge/SiGe MQWs. In the works presented here, my activity was focused on the optimization of growth parameters in order to obtain Ge/SiGe MQW with an high crystal quality. The growth of MQW and their charachterization were performed in the L-NESS laboratory, Politecnico di Milano. The device fabrication and testing were performed by Dr. Papichaya Chaisakul and Mohamed-Said Rouifed at the Institute d'Electronique Fondamentale, University Paris Sud, under the supervision of Dr. Delphine Marris-Morini and Dr. Laurent Vivien. The first goal was the realization of an intensity modulator working at a wavelength of 1.3 μm. We have achieved this goal by choosing an higher Ge content in the virtual substrate, thus increasing the compressive strain in the Ge well. As a consequence, the absorption spectrum of the MQW was shifted toward shorter wavelengths. This work was particularly challenging form the material engineering point of view. In particular, the high content of silicon in the barriers required a careful optimization of the growth temperature in order to suppress the interdiffusion. The second work was focused on the demonstration of the electro-refractive effect in standard $Ge/Si_{0.15}Ge_{85}$ MQWs grown on a $Si_{0.1}Ge_{0.9}$ virtual substrate. In this work, slab waveguides were fabricated and tested in order to characterize the aformentioned effect. An effective refractive index variation up to 1.3×10^{-3} was obtained at moderate applied electric fields. This result may pave the way to the realization of phase modulators based on Ge/SiGe MQWs. The last

MQW-related work focuses on the realization of a photonic interconnection. Our approach is based on the use of the virtual substrate as a low loss waveguide. By choosing a suitable compositional mismatch between the MQW stack and VS, it is possible to minimize the optical losses in the waveguide at the modulation wavelength. A photonic interconnection made by a $Ge/Si_{0.16}Ge_{0.84}$ MQW modulator connected to a $Ge/Si_{0.16}Ge_{0.84}$ MQW photodetector through a $Si_{0.16}Ge_{0.84}$ waveguide was fabricated and tested. This device have shown a great potential for low bit error rate data transimission. Interestingly, the performances of the MQW modulator and photodetector were not affected by the compositional mismatch, if compared to our previous works with strain balanced MQW. The second part of this thesis was focused on the realization of highly strained Ge micro-bridges and on the study of the impact of the growth parameters on the carrier lifetime in Ge-on-Si epilayers. Also in this case, my activity was focused on the material engineering and characterization. The experimental activity was coordinated and supervised by Dr. Hans Sigg, Prof. Ralph Spolenak and Prof. Jerome Faist. The device fabrication and testing was performed by Martin Suess, Richard Geiger and Dr. Renato Minamisawa in ETH Zurich and Paul Scherrer Institute. Tensile strain is a very powerful tool in order to transform germanium into an efficient light emitter. The approach presented here is based on the fabrication of suspended micro-bridges in which the thermal strain, already present in the Ge epilayer before the processing, is strongly enhanced in the constricted region. In this first work, an undoped sample was processed in order to study the effect of high uniaxial strain on the band structure of Ge. By using this powerful top-down fabrication technique, we were able to reach an unixial tensile strain up to 3.1%, the highest reported so far. The aim of the second work was to highlight the role of the growth parameters on the carrier lifetime. Pump-probe transmission spectroscopy was performed on four differently prepared Ge-on-Si and Ge-on-GOI samples in order to investigate the role of doping, thermal annealing and defective Si/Ge interface on the carrier lifetime. We found that thermal annealing perfomed on highly doped sample causes the formation of impurity clusters which are able to

seriously deteriorate the quality of the epilayers. We have also determined that the recombination at defective Ge/Si interface is the dominant cause for the reduction of the carrier lifetime in Ge-on-Si epilayer with respect to the typical lifetime known for bulk germanium.

Bibliography

[1] M. Paniccia *Integrating silicon photonics* Nat. Photon. 4, 498-499 (2010)

[2] http://www.luxtera.com

[3] http://www.kotura.com

[4] D.A.B. Miller *Energy consumption in optical modulators for interconnects* Opt. Expr. 20,A293-A308 (2012)

[5] M. Streshinsky, R. Ding, Y. Liu, A. Novack, Y. Yang, Y. Ma, X. Tu, E.K.S. Chee, A. Eu-Jin Lim, P. Guo-Qiang Lo, T. Baehr-Jones, and M. Hochberg *Low power 50 Gb/s silicon traveling wave Mach-Zehnder modulator near 1300 nm* Opt. Exp. 21, 30350-30357 (2013)

[6] L. Liao, D. Samara-Rubio, M. Morse, A. Liu, D. Hodge, D. Rubin, U.D. Keil, and T. Franck *High speed silicon Mach-Zehnder modulator* Opt. Expr. 13,3129-3135 (2005)

[7] J. Liu, X. Sun, R. Camacho-Aguilera, L. Kimerling, and J. Michel *A Ge-on-Si laser operating at room temperature* Opt. Lett. 35, 679 (2010)

[8] R. Camacho-Aguilera, Y. Cai, N. Patel, J. T. Bessette, M. Romagnoli, L. C. Kimerling, and J. Michel *An electrically pumped germanium laser* Opt. Expr. 20, 11316-11320 (2012)

[9] D.A.B. Miller *Device Requirements for Optical Interconnects to Silicon Chips* Proc. IEEE 97, 1166 - 1185 (2009)

[10] A.L.Washburn,L.C. Gunn,R.C. Bailey,*Label-Free Quantitation of a Cancer Biomarker in Complex Media Using Silicon Photonic Microring Resonators* Anal. Chem. 2009, 81, 94999506

[11] http://newsroom.intel.com

[12] D.A.B. Miller *Device requirements for optical interconnects to silicon chips* Proc. IEEE 97, 1166-1185 (2009)

[13] D.A.B. Miller *Optical interconnects to electronic chips*Appl. Opt. 49, F59-F70 (2010)

[14] L. Chen and M. Lipson *Ultra-low capacitance and high speed germanium photodetectors on silicon* Opt. Expr. 17,108135 (2009)

[15] L. Virot,L. Vivien,J-M. Fdli,Y. Bogumilowicz, J-M. Hartmann,F. Buf,P.Crozat,D. Marris-Morini and E. Cassan *High-performance waveguide-integrated germanium PIN photodiodes for optical communication applications*Photon. Res. 1, 140-147 (2013)

[16] K. Takeda,T. Sato,A. Shinya,K. Nozaki,W. Kobayashi, H. Taniyama,M. Notomi,K. Hasebe, T. Kakitsuka and S. Matsuo *Few-fJ/bit data transmissions using directly modulated lambda-scale embedded active region photonic-crystal lasers* Nat. Phot. 7, 569575 (2013)

[17] S. Schmitt-Rink, D. S. Chemla, W. H. Knox, and D. A. B. Miller *How fast is excitonic electroabsorption?* Opt. Lett. 15, 6062 (1990)

[18] P. Chaisakul, D. Marris-Morini, M.-S. Rouifed, G.Isella, D. Chrastina, J. Frigerio, X. Le Roux, S. Edmond, J.-R. Coudevylle and L. Vivien *23 GHz Ge/SiGe quantum well electro-absorption modulator* Opt. Expr. 20, 3219-3224 (2012)

[19] D. Liang and J.E. Bowers Recent progress in lasers on silicon Nat. Phot. 4, 511-517 (2010)

[20] O.Boyraz and B. Jalali *Demonstration of a silicon Raman laser* Opt. Express 12, 52695273 (2004).

[21] R. Jones, H. Rong, A. Liu, A. W. Fang, and M. Paniccia *Net continuous wave optical gain in a low loss silicon-on-insulator waveguide by stimulated Raman scattering* Opt. Express 13, 519525 (2005)

[22] H.Rong, R. Jones, A. Liu, O. Cohen, D. Hak, A. Fang and M. Paniccia *A continuous-wave Raman silicon laser* Nature 433,725728 (2005)

[23] Y.H. Xie,K. L. Wang and Y.C. Kao, *An investigation on surface conditions for Si molecular beam epitaxial (MBE) growth* J. Vac. Sci. Tech. A 3,10351039 (1985).

[24] Y. Masafumi,S. Mitsuru and I. Yoshio *Misfit stress dependence of dislocation density reduction in GaAs films on Si substrates grown by strained-layer superlattices* Appl. Phys. Lett. 54, 25682570 (1989).

[25] M.E. Groenert et al. *Monolithic integration of room-temperature cw GaAs/AlGaAs lasers on Si substrates via relaxed graded GeSi buffer layers* J. Appl. Phys. 93, 362367 (2003).

[26] G.Roelkens, D. Van Thourhout,R. Baets,R. Notzel and M. Smit *Laser emission and photodetection in an InP/InGaAsP layer integrated on and coupled to a silicon-on-insulator waveguide circuit* Opt. Express 14, 81548159 (2006).

[27] D.Liang et al. *Hybrid silicon (=1.5 mm) microring lasers and integrated photodetectors* Opt. Express 17, 2035520364 (2009).

[28] R.A. Soref and B. Bennet *Electrooptical effects in silicon* IEEE J. Quant. Electron. 23, 123-129 (1987)

[29] A. Liu, R. Jones, L. Liao, D. Samara-Rubio, D. Rubin, O. Cohen, R. Nicolaescu and M. Paniccia *A high-speed silicon optical modulator based on a metaloxidesemiconductor capacitor*Nature 427, 615-618 (2004)

[30] G.T. Reed, G. Mashanovich, F.Y. Gardes and D.J. ThomsonSilicon optical modulators Nat. Phot. 4, 518-526 (2010)

[31] K.Kajikawa,T. Tabei and H. Sunami *An infrared silicon optical modulator of metal.oxide.semiconductor capacitor based on accumulation-carrier absorption* Jpn. J. Appl. Phys. 48, 04C107 (2009).

[32] A. Liu, L. Liao,D. Rubin, H. Nguyen, B. Ciftcioglu, Y. Chetrit, N. Izhaky and M. Paniccia *High-speed optical modulation based on carrier depletion in a silicon waveguide* Opt. Expr. 15, 660668 (2007)

[33] Q.Xu, B. Schmidt,S. Pradhan and M. Lipson *Micrometre-scale silicon electrooptic modulator* Nature 435, 325327 (2005).

[34] M.Soljacic et al. *Photonic-crystal slow-light enhancement of nonlinear phase sensitivity* J. Opt. Soc. Am. B 19, 20522059 (2002).

[35] T.Yin et al. *31 GHz Ge n-i-p waveguide photodetectors on silicon-oninsulator substrate* Opt. Express 15, 1396513971 (2007).

[36] Y. Kang et al. *Monolithic germanium/silicon avalanche photodiodes with 340 GHz gainbandwidth product* Nature Photon. 3, 5963 (2008).

[37] J. Liu, X. Sun, D. Pan, X. Wang, L. C. Kimerling, T. L. Koch, and J.Michel *Tensile-strained, n-type Ge as a gain medium for monolithic laser integration on Si* Opt. Express 15, 1127211277 (2007)

[38] M. E. El Kurdi, T. Kociniewski, T.P. Ngo, J.Boulmer, D. Debarre, P. Boucaud, J.F. Damlencourt, O. Kermarrec and D. Bensahel *Enhanced photoluminescence of heavily n-doped germanium* Appl. Phys. Lett. 94, 191107 (2009)

[39] T.H. Cheng, K.L. Peng, C.Y. Chen, H.S. Lan, Y.R. Wu, C.W. Liu and H.H. Tseng *Strain-enhanced photoluminescence from Ge direct transitions* Appl. Phys. Lett. 96, 211108 (2010)

[40] X. Sun, J. Liu, L.C. Kimerling and J. Michel *Room-temperature direct bandgap electroluminescence from Ge-on-Si light-emitting diode* Opt. Lett. 34,1198-1200 (2009)

[41] J.Liu, M. Beals, A. Pomerene, S. Bernardis, R. Sun, J. Cheng, L.C. Kimerlingh and J. Michel *Waveguide-integrated, ultralow-energy GeSi electro-absorption modulators*Nat. Photon 2, 433-437 (2008)

[42] Y.-H. Kuo, Y. K. Lee, Y. Ge, S. Ren, J. E. Roth, T. I. Kaminis, D.A.B. Miller and J. S. Harris *Strong quantum confined Stark effect in a germanium quantum-well structure on silicon* Nature, 437, 1334-1336 (2005)

[43] Y.-H. Kuo, Y.K. Lee, Y. Ge, S. Ren, J. E. Roth, T. I. Kaminis, D.A.B. Miller and J. S. Harris *Quantum-Confined Stark Effect in Ge/SiGe Quantum Wells on Si for Optical Modulators* IEEE J. Sel. Top. Quantum. Elec. 12, 1503-1513 (2006)

[44] M. Virgilio and G.Grosso *Quantum-confined Stark effect in Ge/SiGe quantum wells: A tight-binding description* Phys. Rev. B 77, 165315 (2008)

[45] D. J. Paul *8-band k.p modeling of the quantum confined Stark effect in Ge quantum wells on Si substrates* Phys. Rev. B 77 155323 (2008)

[46] M. Virgilio, M. Bonfanti, D. Chrastina, A. Neels, G. Isella, E. Grilli, M. Guzzi, G. Grosso, H. Sigg, and H. von Knel*Polarization-dependent absorption in Ge/SiGe multiple quantum wells: theory and experiment* Phys. Rev. B 79, 075323 (2009)

[47] P. Chaisakul, D. Marris-Morini, G. Isella, D. Chrastina, X. Le Roux, S. Edmond, J.-R. Coudevylle, E. Cassan, and L. Vivien *Polarization dependence of quantum-confined Stark effect in Ge/SiGe quantum well planar waveguides* Optics Lett. 36, 1794-1796 (2011)

[48] P. Chaisakul, D. Marris-Morini, M-S. Rouifed, J. Frigerio, G. Isella, D. Chrastina, J.-R. Coudevylle, X. Le Roux, S. Edmond, D. Bouville, and

L. Vivien *quantum-confined Stark effect from light hole related direct-gap transitions in Ge quantum wells* Appl. Phys. Lett. 102, 191107 (2013)

[49] Clayes S.,Simoen E.,*Germanium based technology*, Elsevier, 2007

[50] Kasper E., Paul D.J. ,*Silicon Quantum Integrated Circuits*, Springer, 2005

[51] Bardeen J., Shockley W.,*Deformation Potentials and Mobilities in Non-Polar Crystals*, Phys. Rev., 80, 72-80 (1950)

[52] Van der Walle C.G.,*Band lineups and deformation potentials in model solid theory*, Phys. Rev. B, 39, 1871-1883 (1989)

[53] Cannon D.D., Liu J., Ishikawa J., Wada K., Danielson D.T., Jongthammanurak S., Michel J. and Kimerling L.C.,*Tensile strained epitaxial Ge films on Si(100) substrates with potential application in L-band telecommunications*, Appl. Phys. Lett. 84, 906-908, (2004)

[54] Capellini G., De Seta M., Zaumseil P., Kozlowsky G. and -schroeder T., *High temperature x ray diffraction measurements on Ge/Si(001) heterostructures: A study on the residual strain*, J. Appl. Phys 111, 073518 (2012)

[55] El Kurdi M., Bertin H., Martincic E., de Kersauson M., Fishman G., Sauvage S. Bosseboeuf A. and Bocaud P., *Control of direct gap emission of bulk germanium by mechanical tensile strain* Appl. Phys. Lett. 96, 041909 (2010)

[56] Raja Jain J., Hryciw A., Baer T.M., Miller D.A.B., Brongersma M.L. and Howe R.T. *A micromachining-based technology for enhancing germanium light emission via tensile strain* Nat. Phot. 6, 398-405 (2012)

[57] G. Capellini1, G. Kozlowski, Y. Yamamoto, M. Lisker, C. Wenger, G. Niu, P. Zaumseil, B. Tillack, A. Ghrib, M. de Kersauson, M. El Kurdi, P. Boucaud, and T. Schroeder *Strain analysis in SiN/Ge microstructures*

obtained via Si-complementary metal oxide semiconductor compatible approach J.Appl. Phys. 113, 013513 (2013)

[58] A. Ghrib, M. de Kersauson, M. El Kurdi, R. Jakomin, G. Beaudoin, S. Sauvage,G. Fishman, G. Ndong, M. Chaigneau, R. Ossikovski I. Sagnes, and P. Boucaud. *Control of tensile strain in germanium waveguides through silicon nitride layers* Appl. Phys. Lett. 100, 201104 (2012)

[59] M.G.A. Bernard and G. Duraffourg *Laser conditions in semiconductors* physica status solidi(b) 1, 699-703 (1961)

[60] E. Gaubas and J. Vanhellemont *Dependence of carrier lifetime in germanium on resistivity and carrier injection level* Appl. Phys. Lett. 89, 142106 (2006)

[61] W. G. Spitzer, F. A. Trumbore, and R. A. Logan *Properties of heavily doped n-type germanium*J. Appl. Phys. 32, 18221830 (1961).

[62] J. I. Pankove and P. Aigrain *Optical absorption of arsenic doped degenerate germanium* Phys. Rev. 126, 956962 (1962)

[63] C. Haas, *Infrared absorption in heavily doped n-type germanium* Phys. Rev. 125, 19651971 (1962).)

[64] L. Carroll, P. Friedli, S. Neuenschwander, H. Sigg, S. Cecchi, F. Isa, D. Chrastina, G. Isella, Y. Fedoryshyn, and J. Faist *Directgap gain and optical absorption in germanium correlated to the density of photoexcited carriers, doping, and strain* Phys. Rev. Lett. 109, 057402 (2012).

[65] H. Yaguchi, K. Takemasa, K. Onabe, R. Ito and Y. Shiraki *Characterization of Ge/SiGe strained-barrier quantum well structures using photoreflectance spectroscopy* Phys. Rev. B 49, 7394-7399 (1994)

[66] Y. Miyake, J. Y. Kim, Y. Shiraki and S. Fukatsu *Absence of Stark shift in strained* $Si_{1-x}Ge_x$*/Si type I quantum wells* Appl. Phys. Lett. 68, 2097-2099 (1996)

[67] M. Virgilio and G. Grosso *Type-I alignement and direct fundamental gap in SiGe based heterostructures* J. Phys. Cond. Matter 18, 1021-1031 (2006)

[68] D.A.B. Miller, D. S. Chemla, T.C. Damen, A.C. Gossard, W. Wiegmann, T.H. Wood and C.A. Burrus *Band edge electroabsorption in quantum well structures: The quantum confined Stark effect* Phys. Rev. Lett. 53, 2173-2176 (1984)

[69] J. W. Matthews, A. E. Blakeslee *Defects in epitaxial multilayers - I. Misfit dislocations.*J. Cryst. Growth 27, 118 (1974)

[70] R. People and J. C. Bean *Calculation of critical layer thickness versus lattice mismatch for Ge_xSi_{1-x}/Si strained-layer heterostructures* Appl. Phys. Lett. 47 (3) 322-324 (1985)

[71] H.-C. Luan, D. R. Lim, K. K. Lee, K. M. Chen, J. G. Sandland,K. Wada, and L. C. Kimerling *High-quality Ge epilayers on Si with low threading-dislocation densities* Appl. Phys. Lett. 75, 2909-2911 (1999)

[72] S. Ren, Y. Rong, T. I. Kamins, J. S. Harris, and D. A. B. Miller *Selective epitaxial growth of Ge/Si0.15Ge0.85 quantum wells on Si substrate using reduced pressure chemical vapor deposition* Appl. Phys. Lett. 98, 151108 (2011)

[73] S. Luryi, A. Kastalsky, J. C. Bean*New infrared detector on a silicon chip* IEEE T. Electron Dev. 31 (9) 11351139 (1984)

[74] E. A. Fitzgerald, Y.-H. Xie, M. L. Green, D. Brasen, A. R. Kortan,J. Michel, Y.-J. Mii, B. E. Weir *Totally relaxed Ge_xSi1-x layers with low threading dislocation densities grown on Si substrates* Appl. Phys. Lett. 59 (7) 811813 (1991)

[75] V. A. Shah, A. Dobbie, M. Myronov, D. J. F. Fulgoni, L. J. Nash, and D. R. Leadley *Reverse graded relaxed buffers for high Ge content SiGe virtual substrates* Appl. Phys. Lett. 93, 192103 (2008)

[76] C. Lam *Passive Optical Networks Principles and Practice*, Elsevier, 2007.

[77] L. Lever,Y. Hu,M. Myronov,X. Liu, N. Owens, F. Y. Gardes,I. P. Marko, S. J. Sweeney, Z. Ikoni, D. R. Leadley, G. T. Reed and R. W. Kelsall *Modulation of the absorption coefficient at* $1.3\mu m$ *in Ge/SiGe multiple quantum well heterostructures on silicon* Opt. Lett. 36,4158-4160 (2011)

[78] G. Isella, D. Chrastina, B. Rssner, T. Hackbarth, H-J.Herzog, U. Knig, and H. von Knel *Low-energy plasma-enhanced chemical vapor deposition for strained Si and Ge heterostructures and devices* Solid State Electron.48, 1317-1323 (2004).

[79] J. P. Dismukes, L. Ekstrom, and R. J. Paff *Lattice parameter and density in Germanium-Silicon alloys* J. Phys. Chem 68, 10 (1964).

[80] J. J. Wortman and R. A. Evans *Young's modulus, shear modulus, and Poisson's ratio in Silicon and Germanium* J. Appl. Phys. 36, 153, (1965).

[81] B.S. Meyerson, F.K. LeGoues, T.N. Guen, D.L. Harame, Appl. Phys. Lett. 50 (1997) 113.

[82] F. Schaeffer, Semicond. Sci. Technol. 12 (1997) 1515.

[83] P. Chaisakul, D. Marris-Morini, G. Isella, D. Chrastina, X. Le Roux, E. Gatti, S. Edmond, J. Osmond, E. Cassan, and L. Vivien *Quantum-confined Stark effect measurements in Ge/SiGe quantum-well structures* Optics Letters, 35(17), 2913-2915, (2010).

[84] L.Lever, Z. Ikonic, A. Valavanis, R.W. Kelsall, M. Myronov, D.R. Leadley, Y. Hu, N. Owens, F.Y. Gardes and G.T. Reed *Optical absorption in highly strained Ge/SiGe quantum wells: The role of* Γ-Δ *scattering* J. Appl. Phys. 112, 123105 (2012)

[85] J. Frigerio, P. Chaisakul, D. Marris-Morini, S. Cecchi, M.S. Roufied, G. Isella, L. Vivien *Electro-refractive effect in Ge/SiGe multiple quantum wells* Appl. Phys. Lett. 102, 061102-061102-4 (2013)

[86] J.S. Sites and P.R. Ashley *High-performance Mach-Zehnder modulator in multiple quantum well GaAs/AlGaAs* J. Lightwave Technol. 12, 1167 (1992).

[87] L. Liao, D. Samara-Rubio, M. Morse, A. Liu, D. Hodge, D.Rubin, U.D. Keil and T. Franck *High-speed silicon Mach-Zehnder modulator* Opt. Express 13, 3129 (2005)

[88] 19R. K. Schaevitz,D. S. Ly-Gagnon, J. E. Roth, E. H. Edwards, and D. A. B. Miller *Indirect absorption in germanium quantum wells* AIP Advances 1, 032164 (2011).

[89] J.S. Wiener, D.A.B. Miller and D.S. Chemla *Quadratic electrooptic effect due to the quantumconfined Stark effect in quantum wells* Appl. Phys. Lett. 50, 842 (1987).

[90] L Glick, F. K. Reinhart, G. Weimann, and W. Schlapp *Quadratic electrooptic light modulation in a GaAs/AlGaAs multiquantum well heterostructure near the excitonic gap* Appl. Phys.Lett. 48, 989 (1986).

[91] R. Braunstein, A. R. Moore, and F. Herman*Intrinsic Optical Absorption in Germanium-Silicon Alloys* Phys. Rev. 109, 695710 (1958).

[92] Y. Tang, H.-W. Chen, S. Jain, J. D. Peters, U. Westergren, and J. E. Bowers *50 Gb/s hybrid silicon traveling-wave electroabsorption modulator* Opt. Express 19, 5811-5816 (2011).

[93] M. J. Suess, R. Geiger, R. A. Minamisawa, G. Schiefler, J. Frigerio, D. Chrastina, G. Isella, R. Spolenak, J. Faist and H. Sigg *Analysis of enhanced light emission from highly strained germanium micro bridges* Nat. Phot. 7, 466-472 (2013)

Acknowledgments

The research on Ge/SiGe MQWs has received funding from the French ANR under project GOSPEL (Direct Gap related Optical Properties of Ge/SiGe Multiple Quantum Wells). This work was partly supported by the french RENATECH network.I would like to give credits to the people involved in this project. Dr. Laurent Vivien and Dr. Delphine Marris-Morini for heading and supervising the project. Dr. Papichaya Chaisakul and Mohamed-Said Rouifed for the fabrication and characterization of the devices. The research on highly tensile strained Ge microbridges was partially founded by Swiss National Science Foundation (SNF project no. 130181). I would like to thank Dr. Hans Sigg, Prof. Ralph Spolenak and Prof. Jerome Faist for heading and supervising the project. Martin Suess, Richard Geiger and Dr. Renato Minamisawa for the fabrication and testing of the devices.